

AN ABSTRACT OF THE THESIS

Ludi A. Shadowspeaker for the degree of Master of Science in Material Science presented on August 26, 2003.

Title: On the Fragility and Equilibrium Phases of Metallic Glass Forming Alloys.

Redacted for privacy

Abstract approved

Ralf Busch

The heating rate dependence of the glass transition temperature of the $\text{Ni}_{65}\text{Nb}_{35}$, $\text{Ni}_{60}\text{Nb}_{35}\text{Sn}_5$, $\text{Ni}_{59.35}\text{Nb}_{34.45}\text{Sn}_{6.2}$, $\text{Ni}_{60}(\text{Nb}_{40}\text{Ta}_{60})_{34}\text{Sn}_6$, and $\text{Ni}_{57}\text{Fe}_3\text{Nb}_{35}\text{Sn}_5$ metallic glass forming alloys was investigated with a differential scanning calorimeter (DSC). The inverse heating rate for each DSC experiment was plotted versus inverse temperature and a Vogel-Fulcher-Tamman (VFT) type relation was fit to the data in the plot. The fragilities of the alloys were characterized with the steepness index, m , the fragility parameter D^* , and the VFT temperature, T_0 which are the fit parameters from the VFT relation. It was found that for the binary alloy $D^* = 6.2$, for the ternary alloys $D^* = 11.0$, and that for both the quaternary alloys D^* was about 16. For these alloys, D^* increases linearly as the number of components in the alloy increases.

The fragilities of $Zr_{45.38}Ti_{9.62}Cu_{8.75}Ni_{10}Be_{26.25}$, $Zr_{44}Ti_{11}Cu_{10}Ni_{10}Be_{25}$, $Zr_{42.63}Ti_{12.37}Cu_{11.25}Ni_{10}Be_{23.75}$, $Zr_{41.2}Ti_{13.8}Cu_{12.5}Ni_{10}Be_{22.5}$, $Zr_{39.88}Ti_{15.12}Cu_{13.77}Ni_{9.98}Be_{21.25}$, $Zr_{38.5}Ti_{16.5}Cu_{15.25}Ni_{9.75}Be_{20}$, and $Zr_{46.75}Ti_{8.25}Cu_{7.5}Ni_{10}Be_{27.5}$ were also characterized by the same method. It was found that D^* increases with increasing concentration of Ti and Cu and decreasing concentration of Zr and Be.

The crystalline equilibrium phases of the $Zr_{57}Cu_{15.4}Ni_{12.6}Al_{10}Nb_5$ (Vit 106) bulk metallic glass-forming alloy were determined with electron microprobe analysis (EMPA) and X-ray diffraction (XRD). Five equilibrium phases were found. XRD, EMPA and cluster analysis show that those phases are Zr_2Ni , Zr_2Cu , $ZrCu$, Zr_3Al_2 , and Zr_4Al_3 . All the equilibrium phases, derived from the binary intermetallic compounds, contain the other elements as solutes. In Zr_2Ni and Zr_2Cu , Ni substitutes Cu and vice versa. In $ZrCu$, Ni and Al substitute the Cu. In Zr_3Al_2 and Zr_4Al_3 , Nb substitutes Zr, and Al is substituted by Cu and Ni. This study shows that the additions of 10% Al and 5% Nb are optimum concentrations in the composition space to retard the nucleation and growth of these equilibrium phases when the melt is undercooled.

© Copyright by Ludi A. Shadowspeaker
August 26, 2003
All Rights Reserved

On the Fragility and Equilibrium Phases of Metallic Glass Forming Alloys

By

Ludi A. Shadovspeaker

A THESIS

submitted to

Oregon State University

in partial fulfillment of
the requirements for the
degree of

Master of Science

Presented August 26, 2003

Commencement June 2004

Master of Science thesis of Ludi A. Shadowspeaker presented on August 26, 2003.

APPROVED:

u
u
u
Redacted for privacy

Major Professor, representing Material Science

Redacted for privacy

Coordinator of the Material Science Program

Redacted for privacy

u
Dean of Graduate School

I understand that my thesis will become part of the permanent collection of Oregon State University libraries. My signature below authorizes release of my thesis to any reader upon request.

Redacted for privacy

Ludi A. Shadowspeaker, Author

ACKNOWLEDGEMENTS

The author extends deep gratitude to Dr. Ralf Busch for seeing and nurturing his potential, as well as Isabella Gallino for guiding him. Dr. Alexander Yakochi, Dr. Roger Nielsen, and Minal Shah were instrumental and important to the research describe herein. Tyler Shaw and Ivan McCracken were important role models to me and should be thanked accordingly. The continued and excellent technical support of Chris Way has made my success possible. It is also important to acknowledge the particularly odd circumstances of my life to which I owe a unique perspective; this is both a curse and a blessing.

TABLE OF CONTENTS

1. INTRODUCTION.....	1
2. LITERATURE REVIEW.....	5
3. EXPERIMENTAL METHODS.....	11
3.1 Sample Preparation	11
3.2 Differential Scanning Calorimeter.....	12
3.3 Calibration.....	15
3.4 Preparatory Heat Treatments.....	21
3.5 DSC Experiment.....	22
3.6 Electron Microprobe Analysis.....	23
3.7 X-ray Diffraction.....	24
4. RESULTS.....	25
4.1 Study on the Fragility of Glass Forming Alloys.....	25
4.1.1 DSC Temperature Scans	25
4.1.2 Heating Rate Dependence of T_g and T_x	28
4.1.3 Temperature Dependence of Structural Relaxation Time...	41
4.1.4 Fit to the VFT Relation.....	44
4.2 Study on the Equilibrium Phases of Vit106.....	46
4.2.1 Backscatter Image of Vit 106.....	47
4.2.2 Vit 106 Composition Analysis.....	48
4.2.3 Equilibrium Phases based on Binary Phase Diagrams.....	50
4.2.4 Vit 106 X-ray Diffraction Profile.....	51
DISCUSSION.....	54
5.1 The Supercooled Liquid Region for the Vit 1 Series and Vit 4.....	54
5.2 Heating Rate Dependence of T_g	54

TABLE OF CONTENTS (CONTINUED)

5.3 Fragility Plots	55
5.4 The Effect of Increasing Complexity on D^*	59
5.5 The Effect of Concentration on D^*	62
5.6 Crystal Structure Solubility in Vit 106.....	67
5.7 Diffusion of Al and Nb in Vit 106	67
6. CONCLUSION.....	70
BIBLIOGRAPHY.....	72

LIST OF FIGURES

<u>FIGURE</u>	<u>PAGE</u>
1: DSC output for temperature scan on Vit4.....	3
2: Example fragility or Angell plot.....	10
3: Schematic diagram of the DSC.....	14
4: Melting peak for indium used in calibration.....	17
5: Apparent heating rate dependence of the heat of fusion.....	18
6: Apparent heating rate dependence of the melting temperature of indium	19
7: Apparent heating rate dependence of the melting temperature of zinc.....	20
8: DSC curves for some Nb-Ni based glass forming alloys.....	26
9: DSC curves for some Vit1 series glass forming alloys.....	27
10: Heating rate dependence of temperature for $\text{Ni}_{65}\text{Nb}_{35}$	29
11: Heating rate dependence of temperature for $\text{Ni}_{60}\text{Nb}_{35}\text{Sn}_5$	30
12: Heating rate dependence of temperature for $\text{Ni}_{59.35}\text{Nb}_{34.45}\text{Sn}_{6.2}$	31
13: Heating rate dependence of temperature for $\text{Ni}_{57}\text{Fe}_3\text{Nb}_{35}\text{Sn}_5$	32
14: Heating rate dependence of temperature for $\text{Ni}_{60}(\text{Nb}_{40}\text{Ta}_{60})_{34}\text{Sn}_6$	33
15: Heating rate dependence of temperature for Vit1(-b).....	34
16: Heating rate dependence of temperature for Vit1(-a).....	35
17: Heating rate dependence of temperature for Vit1.....	36
18: Heating rate dependence of temperature for Vit1a.....	37
19: Heating rate dependence of temperature for Vit1b.....	38
20: Heating rate dependence of temperature for Vit1c	39
21: Heating rate dependence of temperature for Vit4.....	40

LIST OF FIGURES (CONTINUED)

<u>FIGURE</u>	<u>PAGE</u>
22: Relaxation time versus temperature the Nb-Ni based alloys.....	42
23: Relaxation time versus temperature the Vit1 series alloys.....	43
24: Backscattering image of slowly cooled Vit 106.....	48
25: Example plot for cluster analysis.....	49
26: X-ray diffraction pattern for crystallized Vit 106.....	52
27: Fragility plot for Nb-Ni based alloys.....	56
28: Fragility plot for Vit1 series alloys.....	57
29: Enhanced view of Fig. 28.....	58
30: D^* versus the number of components in Nb-Ni based alloys.....	60
31: D^* versus the number of components for many alloys.....	61
32: D^* for Vit1 series plotted versus the concentration of Cu.....	63
33: D^* for Vit1 series plotted versus the concentration of Be.....	64
34: D^* for Vit1 series plotted versus the concentration of Ti.....	65
35: D^* for Vit1 series plotted versus the concentration of Zr.....	66

LIST OF TABLES

<u>TABLE</u>	<u>PAGE</u>
Table I: VFT parameters for Nb-Ni based alloys and Vit1 series.....	45
Table II: Equilibrium phases of Vit106	53

1. INTRODUCTION

When a material is cooled beneath its equilibrium melting temperature it can form either a crystalline solid or an amorphous solid. Crystalline solids exhibit long-range order (LRO), they are atomically arranged with periodicity and translational symmetry which occurs on length scales that are much larger than the bond length between the nearest neighbor atoms. That is, the atoms are set in a three-dimensional arrangement that repeats in space. It is possible to avoid crystal formation when cooling by suppressing the diffusion in the material that is necessary to establish LRO. On cooling, the volume of these supercooled liquids continues to decrease. With decreasing temperature the diffusivity in the supercooled liquid become slower and slower so the atoms move less and less. Eventually structural arrest on the timescale of the experiment occurs and the material is an amorphous solid, which is also called a glass. In this study we focus on glass forming alloys that lead to metallic glass formation.

The thermodynamic and mechanical properties of metallic glasses are very different than crystalline metals. For instance, the elastic limit is much higher for metallic glasses than for crystalline metals. Other advantages to metallic glasses include: high toughness, hardness, better soft magnetism, high

corrosion resistance, low coefficient of friction, and high electrical resistance. Novel multicomponent systems of glass forming alloys, such as La-Al-Ni¹, Zr-Ti-Cu-Ni², Zr-Ti-Cu-Ni-Be³, and Zr-Ni-Al-Cu⁴, exhibit very good glass forming ability (GFA). These bulk metallic glasses (BMG) show high thermal stability in their undercooled liquid state with respect to crystallization.

The thermodynamic and kinetic properties of a metallic glass can be determined using a differential scanning calorimeter (DSC), which maps the thermal events of the material. The glass transition temperature, T_g , is defined as the onset of the endothermic DSC event, and the crystallization temperature, T_x , is defined as the onset temperature of the first exothermic DSC event. The supercooled liquid region, ΔT , is the range of temperatures between T_g and T_x . The glass transition region, ΔT_g , is defined as the range of temperatures between the onset and the end of the glass transition. Both heat events, the ΔT , and ΔT_g are illustrated on the DSC curve shown in Fig 1. The viscosity of an alloy at a particular temperature is proportional to its structural (α -) relaxation time, τ , at that temperature. The temperature dependence of τ is easily measured with the heating rate dependence of T_g , and both viscosity and relaxation time obey a Vogel-Fulcher-Tamman (VFT) relation. The fragility concept⁵ is a classification scheme to describe the different temperature dependencies of viscosity. In the VFT relation the VFT-temperature T_0 , the fragility parameter D^* , and the steepness index m , are used to quantify the

connection between τ and the shift of T_g with changing heating rate⁶. Fragility plots are a convenient way to compare the measured viscosities of different glass forming systems. This study focuses first on an Nb-Ni based glass forming system, and second on a Zr-Ti-Cu-Ni-Be glass forming system (Vit1 series). The goal of the first investigation is to describe how D^* changes with the addition of components to the Nb-Ni system. The goal of the second investigation is to describe how D^* changes as the concentration of the components changes in the Vit1 series. The ultimate goal is to investigate the connection between D^* and GFA.

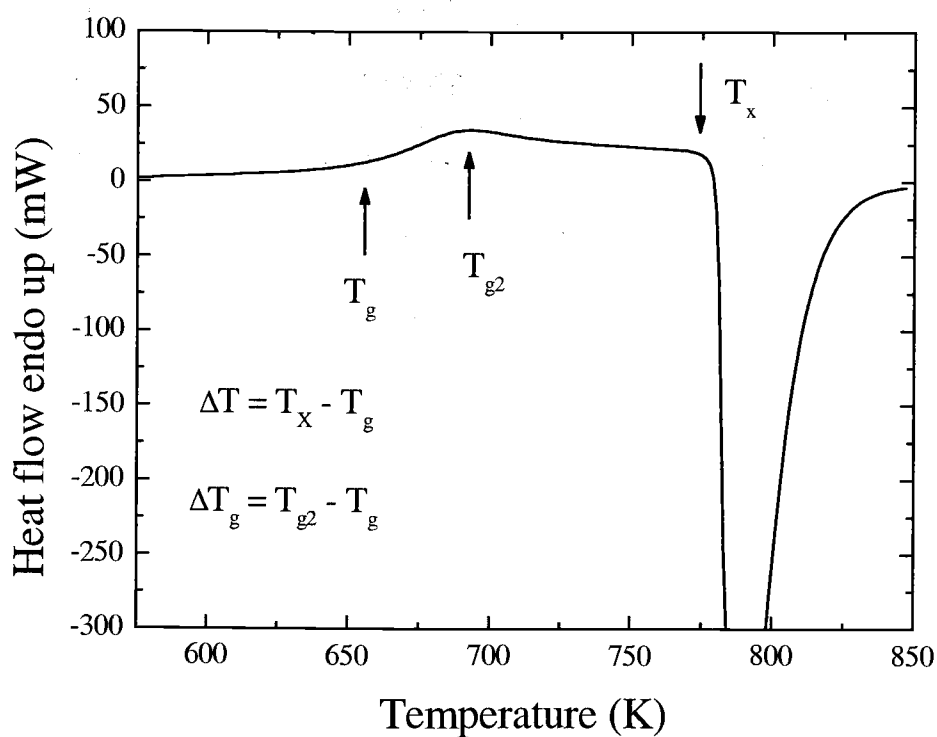


Figure 1: DSC output for temperature scan on Vit 4. T_g , T_x ,

and ΔT_g are shown on the graph.

The third investigation focuses on the $Zr_{57}Cu_{15.4}Ni_{12.6}Al_{10}Nb_5$ (Vit 106) bulk metallic glass-forming alloy⁷. A measure for the GFA of an alloy is its critical cooling rate, which is the slowest rate at which the alloy can be cooled while avoiding crystallization. With a critical cooling rate of 10 Ks^{-1} ⁸, Vit 106 has moderate glass forming ability when compared to $Zr_{41.2}Ti_{13.8}Cu_{12.5}Ni_{10}Be_{22.5}$, which has a critical cooling rate of 1 Ks^{-1} ⁹. Nevertheless, this alloy is important because, with the exception of Pd-Cu-Ni-P^{10,11}, it is the best non-beryllium glass former to date. In addition, Vit 106 is technologically more interesting than Pd-Cu-Ni-P because it is less expensive. The goal of this investigation is to determine the structure and composition of the crystalline equilibrium phases of the Vit 106 alloy. A maximum of five crystalline equilibrium phases is expected because there are five components in the alloy.

2. LITERATURE REVIEW

The first metallic glass, $\text{Au}_{75}\text{Si}_{25}$, was investigated by Duwez¹² in 1960 using a method of rapid quenching with a cooling rate of 10^6 Ks^{-1} . Since Inoue and co-workers discovered metallic glass-forming alloys with critical cooling rates of 10^2 Ks^{-1} in the early 1990's¹³, many metallic glass-forming alloys have been discovered. The Zr-Ti-Cu-Ni-Be alloy introduced by Peker and Johnson³ was one such discovery. As mentioned before this Zr- based alloy has a very low critical cooling rate⁹. The better metallic glass-forming alloys have slower critical cooling rates, and the compositions of those alloys are strongly related to deep eutectics¹⁴. Inoue suggested three rules for glass formation in metallic systems¹⁵. First, the alloys must consist of at least three elements. Second, the atomic sizes of the elements should have at least 12% difference between the largest and the smallest atom. Third, the elements must have a large negative heat of mixing. A.L. Greer also discusses the first and second rule¹⁶. For the purposes of this study, it is useful to review how the temperature dependence of viscosity and relaxation time for glass-forming alloys has been treated in previous literature.

In 1967 Chen and Turnbull established that the $\text{Au}_{77}\text{Ge}_{13.6}\text{Si}_{9.4}$ amorphous alloy is relatively soft in the temperature range of the glass transition and that it flows when a stress is applied to it¹⁷. The same alloy is hard and brittle below the glass transition temperature or after crystallization. The viscosity of

this alloy increases rapidly with falling temperature and can be described by the equation,

$$\eta = 0.52 \exp[1360/(T-241.3)] P. \quad (1)$$

Where P is the unit poise and corresponds to the pre-exponent, T is the temperature, and the numbers are also temperatures. Cohen and Turnbull showed that an equation of the form of Eq. 1 can be derived from the idea that some critical local concentration of the free volume must be achieved in order for flow to occur. The surplus volume in one part of the liquid becomes available to another part without activation energy. Molecular transport occurs by movement of molecules into the voids formed by the redistribution of free volume. The free volume in liquids decreases with falling temperature and at some low temperature is expected to disappear. Thus near the glass transition temperature the probability of the appearance of this critical free volume is negligible.

Since the structural relaxation time describes the relaxation by diffusion of structural modes represented by the variation of free volume it should have the same temperature dependence as the shear viscosity. The structural relaxation time can therefore be expressed with the Doolittle equation.

$$\tau(T) = \tau_0 \exp(V_m/V_f) \quad (2)$$

where V_f is the free volume and V_m is the minimum volume for flow. This establishes that the same processes of microscopic movement underlie self-diffusion, viscosity, and structural relaxation. In the case of a constant thermal expansion coefficient Eq. 2 is equivalent to the VFT equation which is explained later in this section. Cohen and Grest¹⁸ expanded this idea by incorporating ideas from percolation theory¹⁹.

It is found experimentally that when the heating or cooling rate increases in magnitude, the value of T_g also increases. For instance, the higher the cooling rate, the earlier the enthalpy departs from its equilibrium value, and the higher T_g will be. On the other hand, a smaller cooling rate allows the material to stay in the supercooled liquid state until lower temperatures. Typically, the dependence of T_g upon cooling rate is relatively weak; an order of magnitude change in cooling rate may change T_g by only 3-5 K. The logarithm of the cooling rate varies linearly with the glass transition temperature. With the assumption that the volume and enthalpy of the nonequilibrium glass will relax to the value of the metastable supercooled liquid in the limit of infinitely slow cooling, the results of heating rate dependence can also be interpreted. The essential features that relate the dependence of T_g on rate of temperature change to the temperature dependence of the structural relaxation time was first presented by Ritland²⁰. The heating rate dependence of T_g reflects the temperature dependence of the structural relaxation time near T_g , which relates to the temperature dependence of viscosity.

Vogel²¹ and Fulcher²² first observed that in the high-temperature, low viscosity regime, η could be fitted to a form

$$\eta = \eta_0 \exp(b/(T-T_0)) \quad (3)$$

where η_0 , b , and T_0 are constants. This form works well in the low-viscosity region between 10^4 to 10^6 P for most glasses. Some glasses such as SiO_2 and GeO_2 follow an Arrhenius behavior,

$$\eta = \eta_0 \exp(b/T) \quad (4)$$

over the entire range of temperatures. Equation 4 can be written in the form

$$\eta = \eta_0 \exp(D^*T_0/(T-T_0)) \quad (5)$$

where the parameter D^* controls how closely the system obeys the Arrhenius law. Equation 5 is more robust than Eq. 2 because it can also be derived from the configurational entropy theory of Adams and Gibbs²³.

The viscosity of a liquid is a macroscopic measure of its resistance to flow. Figure 2 shows the logarithm of viscosity as a function of temperature for two liquids which are easily supercooled: o-terphenyl and SiO_2 . In Fig 2, the

viscosity of both materials is plotted versus inverse temperature. The inverse temperature is standardized by the glass transition temperature for each of the materials so that T_g for each of the liquids occurs at one on the horizontal axis. This type of plot is called a fragility (or Angell) plot. The viscosity at T_g is typically near 10^{13} P. In this plot this value of viscosity is used to define T_g . The timescale for molecular motion increases dramatically as a supercooled liquid is cooled toward T_g .

The two liquids shown in Fig. 2 have different temperature dependencies as T_g is approached. The viscosity of SiO_2 has an almost Arrhenius dependence while the viscosity for o-terphenyl is non-Arrhenius. On this type of plot, almost all materials would fall in between these two curves. On the basis of this property and others, supercooled liquids have been classified as strong or fragile. Strong liquids like SiO_2 show Arrhenius relaxation processes and typically have three-dimensional network structures of covalent bonds. Fragile liquids like o-terphenyl have quite non-Arrhenius relaxation properties and typically consist of molecules that interact non-directionally²⁴. Pure metals are fragile liquids, but certain alloys exhibit stronger liquid behavior, and some alloys show stronger liquid behavior than others. This investigation was pursued with this in mind.

Relaxation time or inverse heating rate can replace viscosity on a graph like Fig 2 because of their phenomenological connection. We suspect that there may be a connection between strong liquid behavior and the GFA of an alloy.

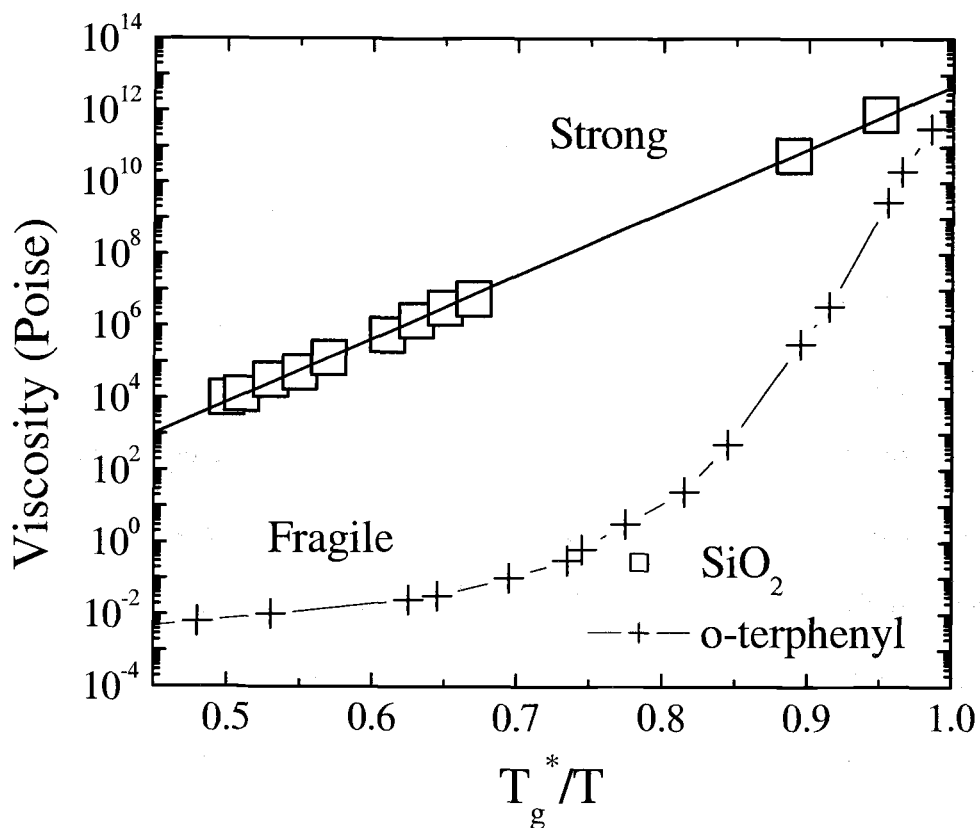


Figure 2: Viscosity versus inverse temperature standardized by the glass transition temperature (fragility or Angell Plot). Examples of strong (SiO_2) and fragile (o-terphenyl) liquid behavior are shown.

3. EXPERIMENTAL METHODS

3.1 Sample Preparation

Three types of metallic glass forming alloys are included in this study. The first set of alloys studied are the Nb-Ni based: $\text{Ni}_{65}\text{Nb}_{35}$, $\text{Ni}_{60}\text{Nb}_{35}\text{Sn}_5$, $\text{Ni}_{59.35}\text{Nb}_{34.45}\text{Sn}_{6.2}$, $\text{Ni}_{60}(\text{Nb}_{40}\text{Ta}_{60})_{34}\text{Sn}_6$, $\text{Ni}_{57}\text{Fe}_3\text{Nb}_{35}\text{Sn}_5$. The second set of alloys studied is the Vit 1 series alloys: $\text{Zr}_{45.38}\text{Ti}_{9.62}\text{Cu}_{8.75}\text{Ni}_{10}\text{Be}_{26.25}$ (Vit1c), $\text{Zr}_{44}\text{Ti}_{11}\text{Cu}_{10}\text{Ni}_{10}\text{Be}_{25}$ (Vit1b), $\text{Zr}_{42.63}\text{Ti}_{12.37}\text{Cu}_{11.25}\text{Ni}_{10}\text{Be}_{23.75}$ (Vit1a), $\text{Zr}_{41.2}\text{Ti}_{13.8}\text{Cu}_{12.5}\text{Ni}_{10}\text{Be}_{22.5}$ (Vit1), $\text{Zr}_{39.88}\text{Ti}_{15.12}\text{Cu}_{13.77}\text{Ni}_{9.98}\text{Be}_{21.25}$ (Vit1(-a)), $\text{Zr}_{38.5}\text{Ti}_{16.5}\text{Cu}_{15.25}\text{Ni}_{9.75}\text{Be}_{20}$ (Vit1(-b)). $\text{Zr}_{46.75}\text{Ti}_{8.25}\text{Cu}_{7.5}\text{Ni}_{10}\text{Be}_{27.5}$ (Vit 4) was included in the analysis of the Vit1 series for comparison. The third study was of a single alloy $\text{Zr}_{57}\text{Cu}_{15.4}\text{Ni}_{12.6}\text{Al}_{10}\text{Nb}_5$ (Vit 106).

There are several methods of producing metallic amorphous solids, such as sputtering thermal evaporation, or melt quenching. Before quenching, a homogeneous mixture of the elements called a master alloy is formed. Master alloys were prepared by arc melting a mixture of the elements having a purity of 99.7 at% or better on a water-cooled copper boat under a Ti-gettered argon atmosphere. Amorphous $\text{Ni}_{65}\text{Nb}_{35}$ ribbons were prepared by rapid quench in a melt spinner. To obtain glassy specimens the other alloys were remelted under vacuum in a quartz tube using an rf induction coil and, except for Vit

106, subsequently injection cast with argon into a copper mold. To avoid contamination, the molten metals were held in the quartz tube for only 10 s.

DSC experiments were performed on all the alloys of the study with the exception of Vit 106. Samples of Ni₆₅Nb₃₅ were cut by hand from the melt-spun ribbons. The other alloys were cut with a Buehler Isomet 1000 precision saw.

3.2 Differential Scanning Calorimeter

In the differential scanning calorimeter (DSC), a sample and an inert reference material are subjected to an identical thermal treatment. In the case of a reaction or transformation in the sample, a heat flux is generated that corresponds to the energy associated with the type of transition. An exothermic event, such as crystallization, is detected in the DSC by the decrease in heat flow that originates in the heat of fusion that is released by the material during crystallization. Likewise an endothermic event, such as melting, is detected in the DSC by the increase in heat flow that corresponds to the heat of fusion absorbed by the material. The DSC produces heat flow versus temperature curves whereby these thermal effects are represented by peaks, or in the case of the glass transition, smoother thermal transitions. By changing the heating rate in the DSC these thermal effects can be measured at

different time scales. In this way it is possible to characterize the kinetic parameters that correspond to these thermal events both qualitatively and quantitatively. In this work, a Perkin Elmer Pyris DSC1 is used to determine the temperature dependence of the structural (α -) relaxation time for the twelve metallic glass-forming alloys listed above.

The DSC has two platinum furnaces that are thermally isolated. The sample furnace holds a test specimen that is held in a sample pan, and a lid of the same material as the pan covers the sample. The reference furnace holds an empty pan and lid²⁵. The sample and reference are thermally insulated with respect to each other. Each furnace is individually heated, and both furnaces are kept at the same temperature. The two-furnace setup is used to enhance the sensitivity of the measurement. The signal produced by the DSC for analysis is the heat flow difference between the two furnaces. For dynamic experiments, the signal is the difference in heat flow input required to keep the furnaces at the same temperature. The intensity of the signal from the DSC is proportional to both the heating rate and the sample mass. A schematic diagram of the DSC is shown in Fig. 3.

To avoid oxidation during the measurements, both pans are kept in an argon atmosphere. For experiments in which it was not necessary for the temperature to exceed 873 K, aluminum pans were used to hold the samples. These Al pans weigh 17.5 mg, and melt at 933 K. For experiments in which it

was necessary for the temperature to exceed 873 K copper pans were used to hold the samples. These Cu pans weigh 51.8 mg, and melt at 1358 K. The melting temperature of Pt is 2045 K.

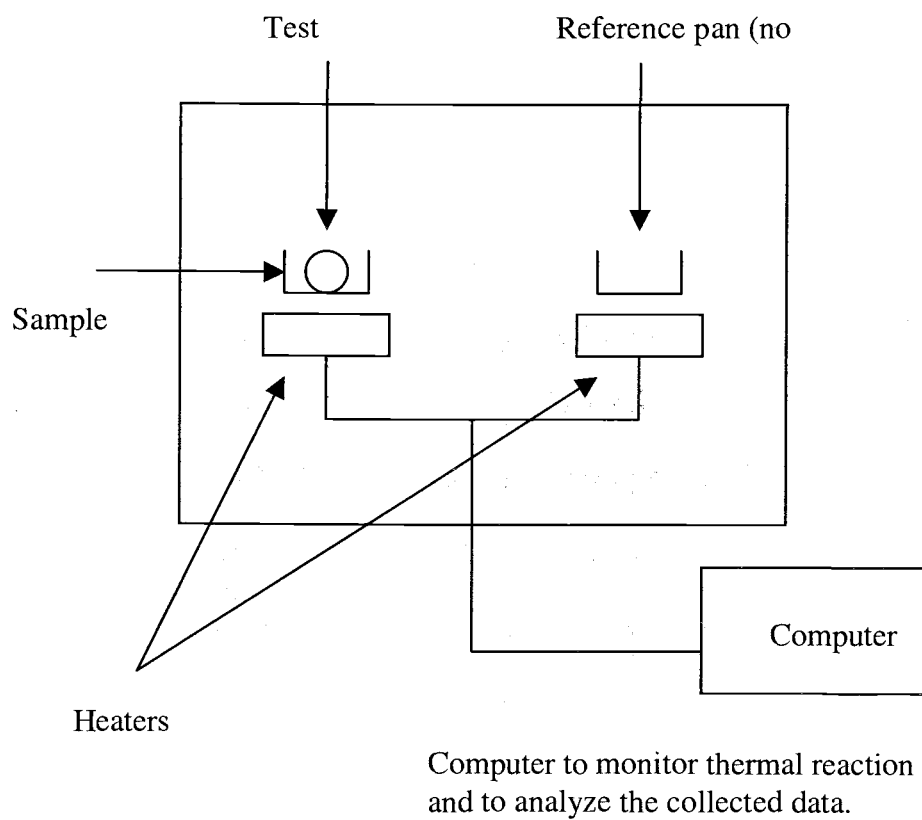


Figure 3: Schematic diagram of the DSC

3.3 Calibration

To ensure that equipment produces accurate measurements it is necessary to calibrate those measurements against known standards. When the DSC is run without samples or sample pans, it produces a signal called the baseline that is particular to the machine itself. The baseline is influenced by the condition of the platinum furnaces and the heaters that are associated with them. It represents the difference between the thermal characteristics of the two furnaces. For instance, it is common that the furnaces will react with samples, sample pans, and particles of the environment. Over time this contamination will affect the baseline. The equipment manufacturers usually perform the initial baseline calibration, but it is necessary to recalibrate the DSC when it is moved, or when significant contamination occurs on the furnace. Additionally, periodic recalibration of the baseline is necessary to insure the integrity of the data the DSC collects. The baseline was corrected prior to these experiments however this calibration is optimal only at a heating rate of 0.333 Ks^{-1} .

The baseline will fluctuate with heating rate, and this is associated with the heat flow and temperature measurement devices. For instance, at high heating rates the temperature of the furnaces is changing faster than the thermal couple can detect. Thus, the baseline will show heating rate dependence and it is necessary to correct for this by calibrating the temperature and heat flow

for different heating rates. The temperature is calibrated by measuring the melting temperature of high purity metals. The peak temperature and peak areas are then determined and serve as calibration parameters for the software. For this DSC, indium and zinc were used as low temperature and high temperature calibration standards respectively. The calibration of the temperature is based on the determination of the extrapolated peak onset temperature, measured at different heating rates. The difference between the observed value at that heating rate and the known calibration values is attributed to the heating rate dependence of the machine, and this difference is compensated for in the software. The temperature calibration was performed for different heating rates, from 0.0333 to 3.33 Ks⁻¹ using indium and zinc standards with a high purity of 99% to 99.999%. The indium was heated from 323 to 473 K and the zinc was heated from 473 to 773 K to determine the apparent heating rate dependence of the melting temperature. The onset of the melting peak is used as the melting temperature for indium and zinc as a function of heating rate. A typical melting peak for indium is shown in Fig. 4. The heat flow is calibrated by measuring the enthalpy of the fusion, ΔH_f for indium at different heating rates. ΔH_f was determined with the peak area, which is the area beneath the melting peak on a heat flow versus time curve and divided by the sample mass. The apparent ΔH_f of indium shifts linearly with changing heating rate as can be seen in Fig. 5. The software compensates for this apparent heating rate dependence of ΔH_f . The result of the calibration data for zinc and indium were plotted and extrapolated to

determine the relation of heating rate and the shift of melting temperature and enthalpy. Figures 6 and 7 show the linear fit for the shift in temperature for indium and zinc, respectively.

This calibration is extremely important for analysis that includes the shift of transition temperatures with heating rate. For instance if a shift in T_g is observed with a bad temperature calibration it will include some shift that is an artifact of the DSC, and analysis based on this observation will be in error.

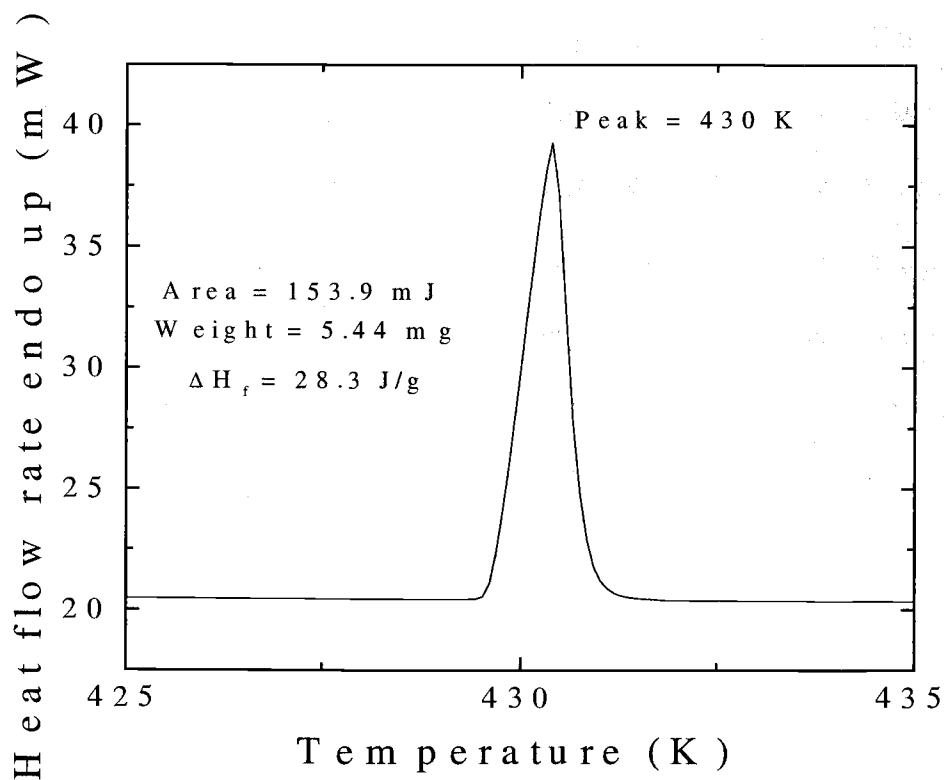


Figure 4: DSC scan for an enthalpy measurement of indium. The peak area indicates the enthalpy of fusion.

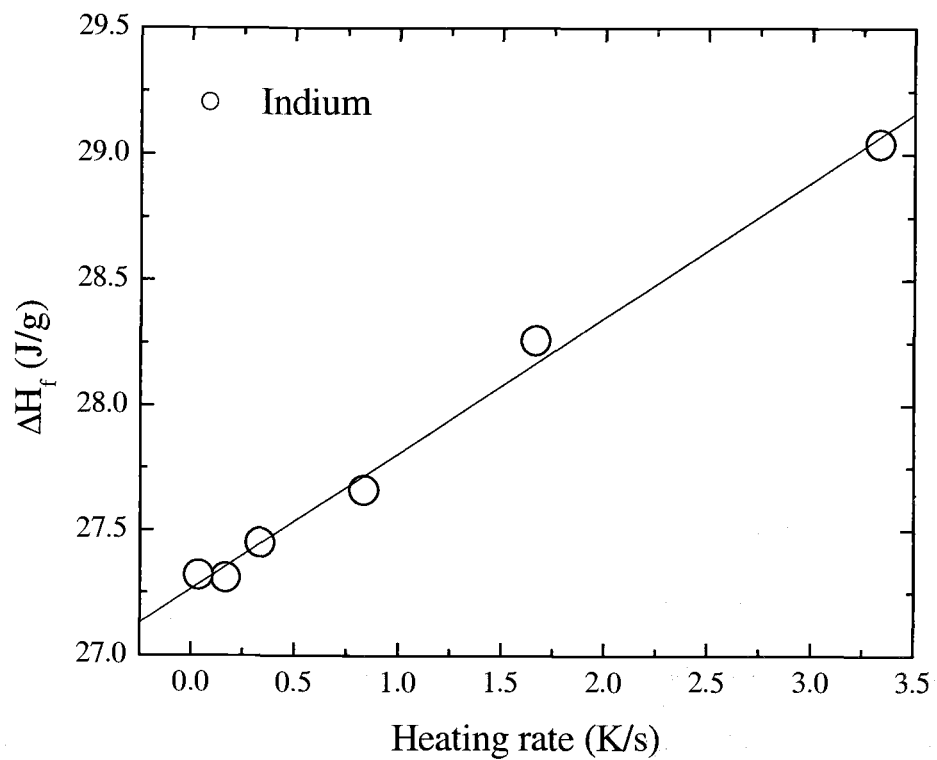


Figure 5: The calibration data for the enthalpy of an indium standard

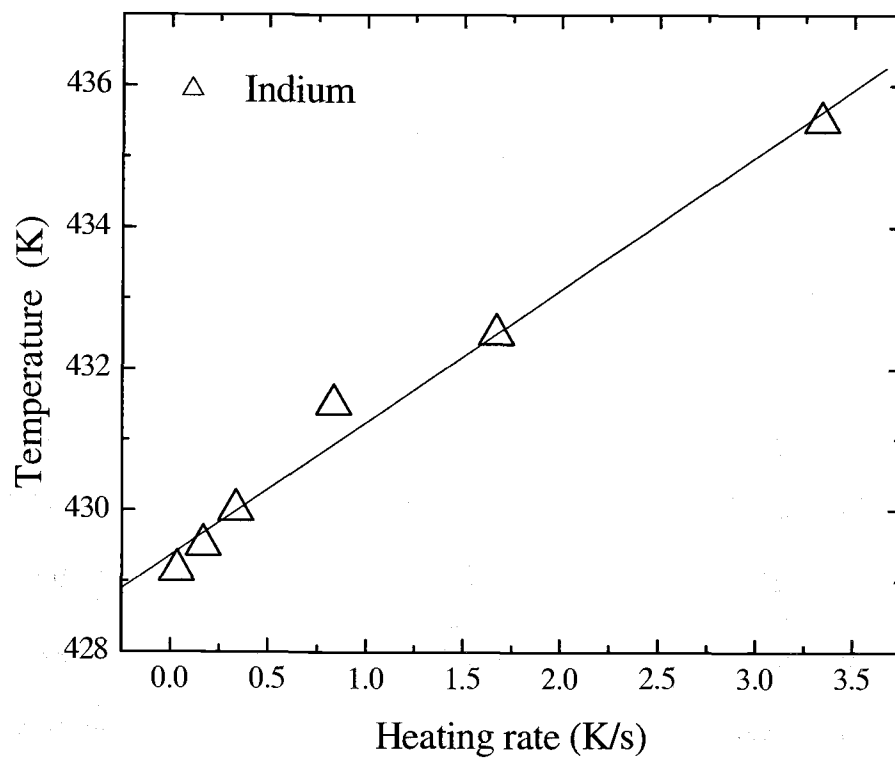


Figure 6: The temperature calibration data for an indium standard

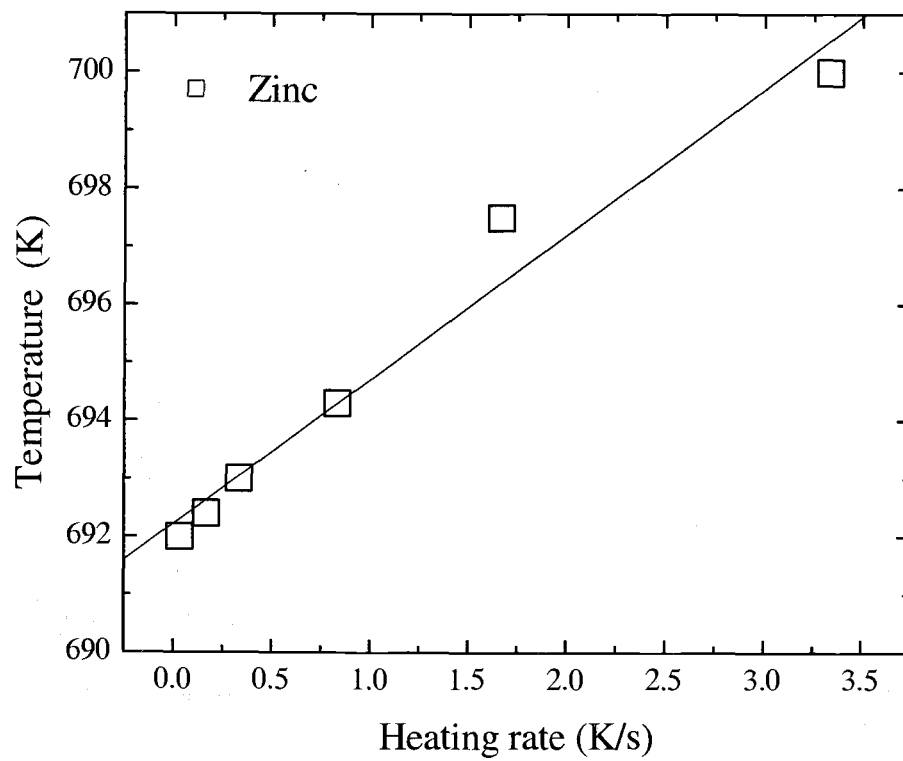


Figure 7: The temperature calibration data for the zinc standard

3.4 Preparatory Heat Treatments

With the DSC, it is possible to heat alloys from the glassy state into the supercooled liquid state and subsequently cool them without crystallization. Heating the samples to a fixed temperature in the supercooled liquid region and cooling them below the glass transition with a well defined heating and cooling rates is called a preheat treatment. This treatment assures that the samples have the same thermal history. When samples of the same alloy come from different stocks, it is desirable to standardize the specimens with by preheating them. In these experiments the preheat temperature was determined by $T_g + (T_x - T_{g2})/3$, it is one third of the way into the supercooled liquid region. It is necessary to heat the sample into the supercooled liquid region in order to erase its prior thermal history, however the precise preheat temperature can be arbitrarily selected as long as it is chosen in a consistent manner. A preheat is most successful in alloys that show a substantial supercooled liquid region when heated from the glassy state. The preheat treatment has a noticeable effect on the thermal properties of the material. That is a sample that has been preheat treated can show transition temperatures that are quite different than the a sample of the same alloy that has not been preheat treated.

The Vit 106 was cooled from the melt state at 1103 K to room temperature with a cooling rate of 0.12 Ks^{-1} . This rate is 2 orders of magnitude below the

critical cooling rate for this alloy, which ensures that the sample would be fully crystallized with a coarse microstructure. The sample was cut with a Buehler Isomet 1000 precision saw and embedded in phenolic epoxy before polishing.

3.5 DSC Experiment

The Nb-Ni based glass forming alloys show values of T_g and T_x above 873 K, so it was necessary to use Cu sample pans instead of Al pans. Samples were heated in the DSC between 573 K and 1023 K at heating rates between 0.0167 Ks^{-1} and 3.33 Ks^{-1} . The masses of the $Ni_{65}Nb_{35}$ samples were limited by the size of the sample pans because the material was from melt spun ribbons. The $Ni_{65}Nb_{35}$ was tested at only four heating rates because these low mass samples did not yield readable heat flow versus temperature signals at low heating rates. The Vit1 series glass forming alloys show values of T_g and T_x below 873 K, so the Al sample pans were used. Samples were heated in the DSC between 473 K and 853 K at heating rates between 0.0167 Ks^{-1} and 3.33 Ks^{-1} . T_g was recorded for each heating rate because the heating rate dependence of the glass transition temperature is used to represent the temperature dependence of τ .

3.6 Electron Microprobe Analysis

The Vit 106 alloy was examined using an electron microprobe, with a 49.9 nA beam current, 15.1 kV accelerating voltage, take off angle of 40°, tilt and azimuth angles of 0°. The signal for each element in the alloy was calibrated against pure samples of the same element for all elements but Al. Al was calibrated against corundum (Al_2O_3) because corundum is more stable with respect to oxidation and easier to polish. Images were obtained in the microprobe by backscattering electrons. A 2 μm diameter electron beam scanned the sample, and the data points were grouped into categories of similar composition. These groups of similar composition were tested for distinctness using the cluster analysis method. In this method the atomic percent (at %) of one component is plotted against the at% of one other component. If the categories are separated on the plot by three standard deviations, then the categories are considered to be distinct. The standard deviations were determined by repeatedly reading the composition of the sample while the electron beam was focused in one location. The composition in that location does not change, so the variation in the reading corresponds to the accuracy of the microprobe. Categories that are distinct with one component plotted against one other may not show the same distinctness in different components. In order to find all of the distinct categories it was necessary to plot each one of the elements in the system against each one of the others.

3.7 X-ray Diffraction

The Vit 106 sample was subsequently analyzed by X-ray diffraction. The specimen was polished again to remove oxides. The data were collected on a Bruker D5000 diffractometer using Cu K- α radiation and a (Li)Si detector with energy discrimination electronics, using 20mm variable incident and antiscatter slits and a 0.2mm detector slit. The instrument was operated in scanning mode with data binned into 0.02° steps and a counting time of 20 seconds per step. The sample was scanned between 20° and 70° in 2θ . The long scan was performed in order to increase the signal to noise ratio.

4. RESULTS

4.1 Studies on the Fragility of Glass Forming Alloys

This portion of the study compares the fragility of five alloys that differ in number of components. It also compares seven alloys that have the same number of components but vary significantly in concentration. We expect to show that the fragility of an alloy is dependent on the number of different size atoms that it involves. We also expect to show that the fragility of an alloy is dependent on the concentration of those elements.

4.1.1 DSC Temperature Scans

Figure 8 shows the heat flow versus temperature curves obtained in the DSC with a heating rate of 0.333 K s^{-1} for the $\text{Ni}_{65}\text{Nb}_{35}$, $\text{Ni}_{59.35}\text{Nb}_{34.45}\text{Sn}_{6.2}$, and the $\text{Ni}_{60}(\text{Nb}_{40}\text{Ta}_{60})_{34}\text{Sn}_6$ alloys. The supercooled liquid region is the range of temperatures between T_g and T_x . This region is very small for the binary alloy, somewhat larger for the ternary alloy, and substantially larger for the quaternary alloy shown in Fig. 8. The $\text{Ni}_{59.35}\text{Nb}_{34.45}\text{Sn}_{6.2}$ alloy exhibits a lower T_g and a lower T_x when it is heated from the glassy state than the $\text{Ni}_{65}\text{Nb}_{35}$ alloy exhibits when it is heated from the glassy state. On the other hand, The $\text{Ni}_{60}(\text{Nb}_{40}\text{Ta}_{60})_{34}\text{Sn}_6$ alloy exhibits a higher T_g and a higher T_x when it is

heated from the glassy state than the $\text{Ni}_{65}\text{Nb}_{35}$ alloy exhibits when it is heated from the glassy state.

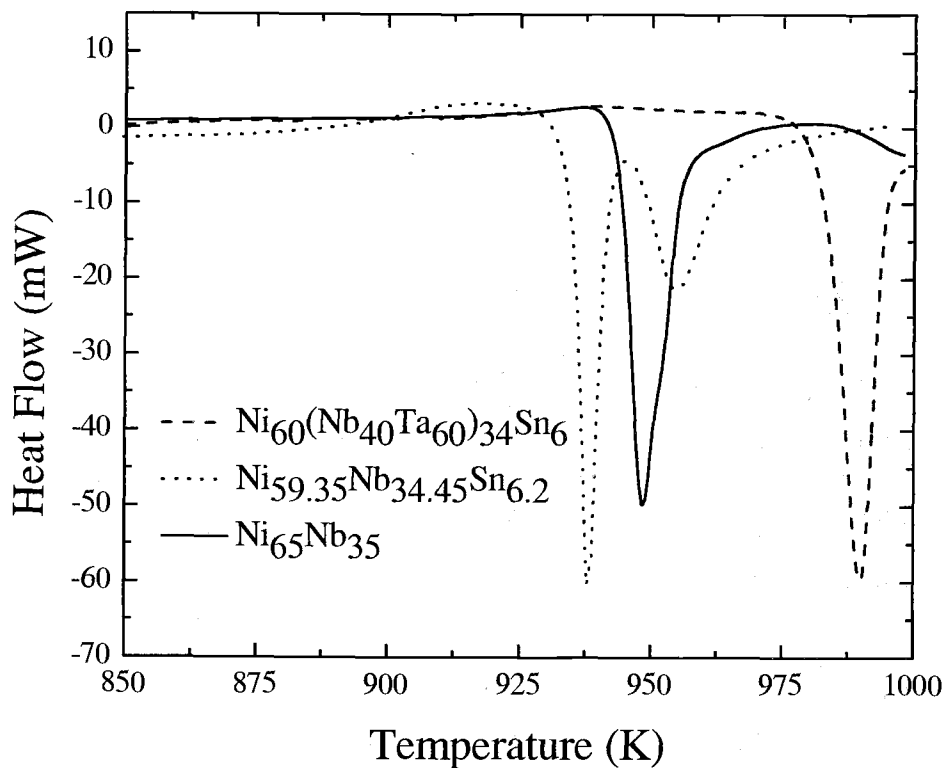


Figure 8: A DSC temperature scan comparing a binary, ternary, and quaternary Nb-Ni based glass forming alloys.

Figure 9 shows the heat flow versus temperature curves obtained in the DSC with a heating rate of 0.333 Ks^{-1} for the Vit1c, Vit1 and Vit1(-b) alloys. The supercooled liquid region is between 629 and 761 K for the Vit1c alloy,

between 636 and 720 for the Vit1 alloy, and between 642 and 691 K for the Vit1(-b) alloy. Vit1c exhibits a lower T_g but a higher T_x when it is heated from the glassy state than the Vit1 exhibits when it is heated from the glassy state. Likewise, Vit1 exhibits a lower T_g but a higher T_x when it is heated from the glassy state than the Vit1(-b) exhibits when it is heated from the glassy state.

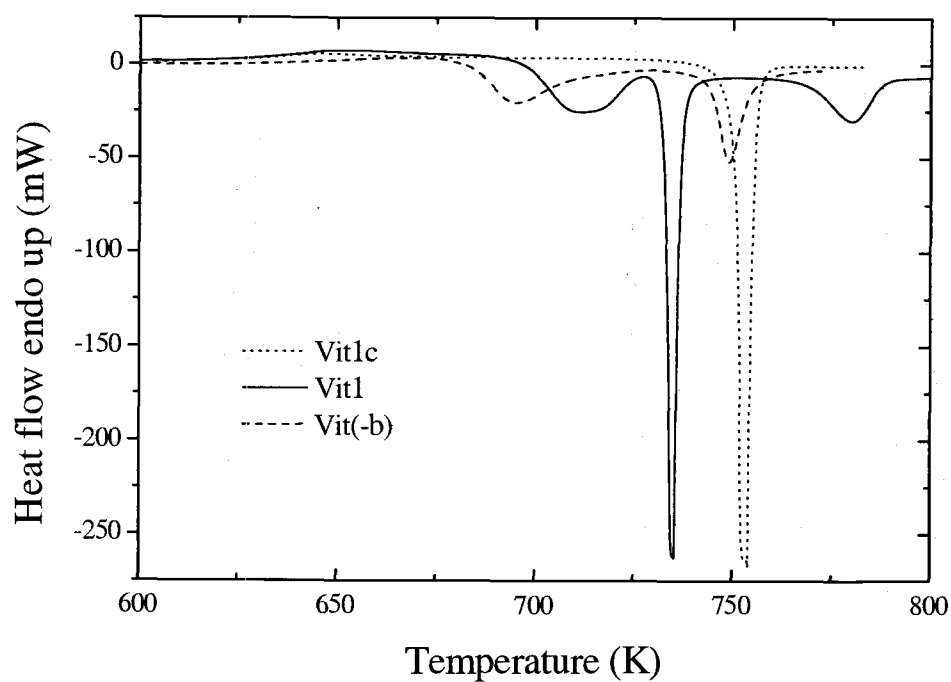


Figure 9: DSC temperature scan comparing a Vit1c, Vit1, and Vit1(-b) glass forming alloys.

4.1.2 Heating Rate Dependence of T_g and T_x

Figures 10 to 21 show the onsets of T_g and T_x from the continuous heating curves for the twelve alloys that were studied in the DSC. They are the calorimetrically observed T_g and T_x for the different alloys plotted versus the heating rate of the DSC. It can be seen in Figs. 10 to 14 that for the Nb-Ni based alloys the change in T_g for changing heating rate is small for the binary alloy, larger for the ternary alloys, and the largest for the quaternary alloys. The supercooled liquid region is the range of temperatures between T_g and T_x . It can be seen in Figs. 10 to 14 that this region is smallest for the binary alloy, larger for the ternary alloys and the largest for the quaternary alloys.

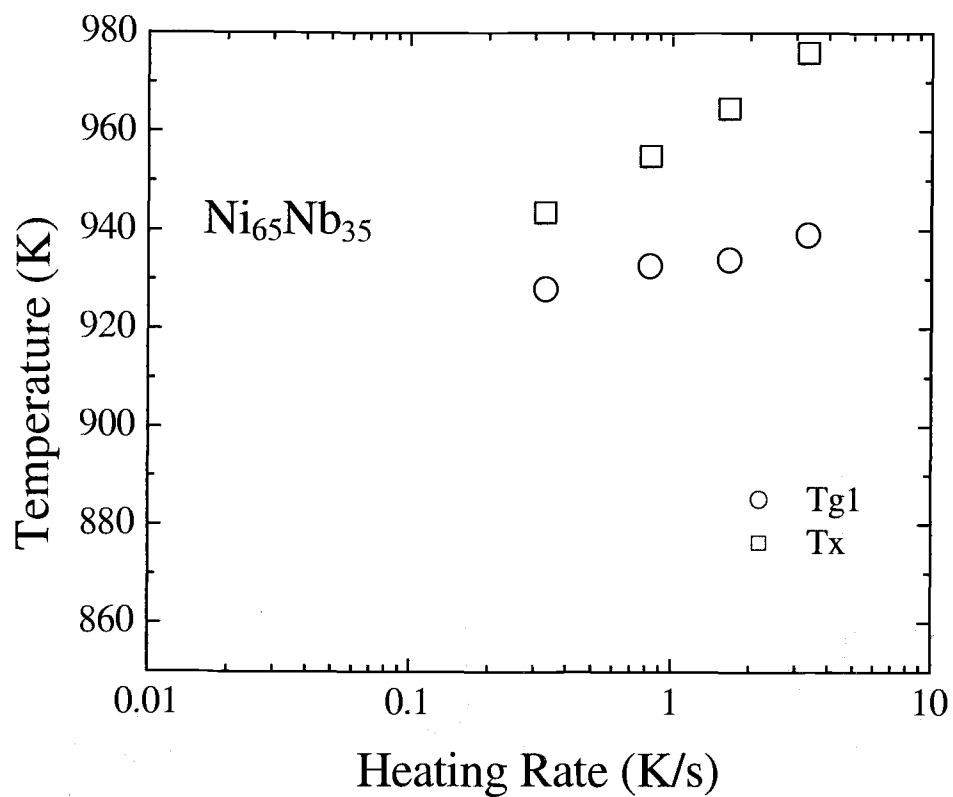


Figure 10: Onsets of glass transition temperature, T_{g1} , and crystallization temperature, T_x , from the continuous heating curves for $Ni_{65}Nb_{35}$

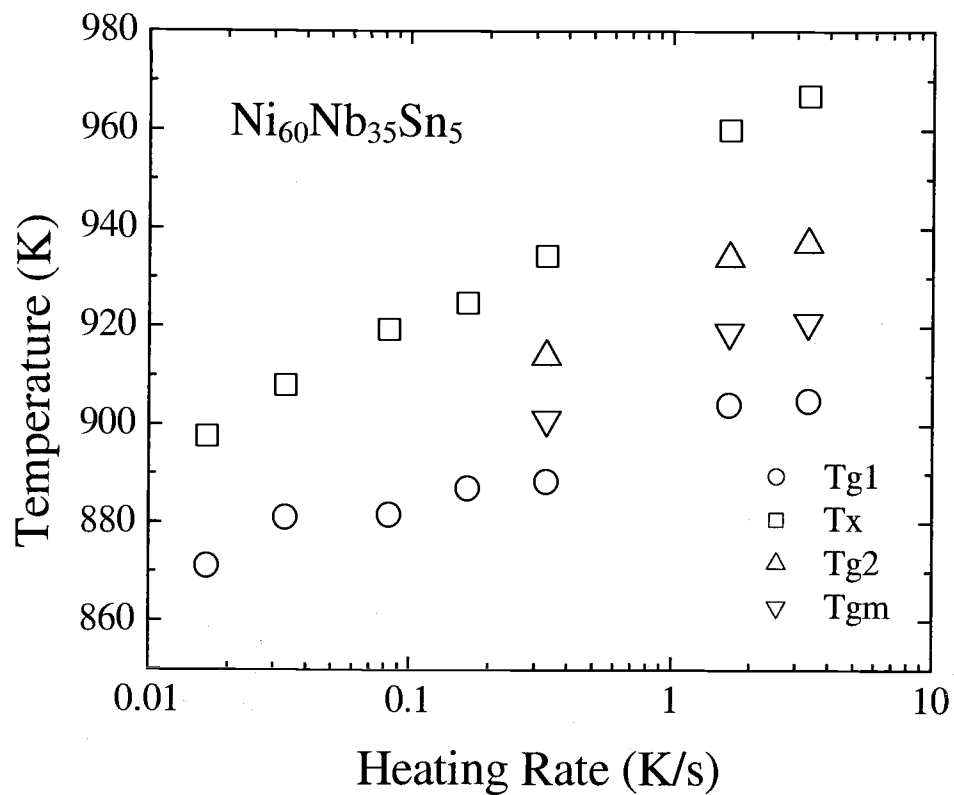


Figure 11: Onsets of glass transition temperature, Tg1, crystallization temperature Tx, the end glass transition temperature, Tg2, and the temperature midway between Tg1 and Tg2, Tgm, from the continuous heating curves for $\text{Ni}_{60}\text{Nb}_{35}\text{Sn}_5$.

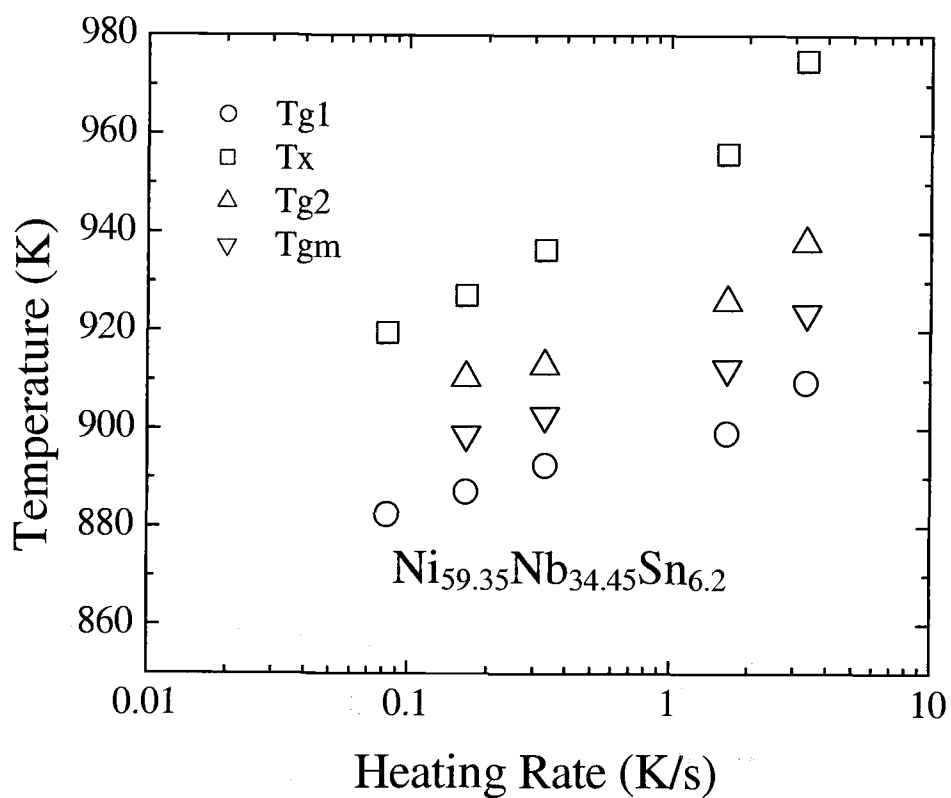


Figure 12: Onsets of glass transition temperature, Tg1, crystallization temperature Tx, the end glass transition temperature, Tg2, and the temperature midway between Tg1 and Tg2, Tgm, from the continuous heating curves for



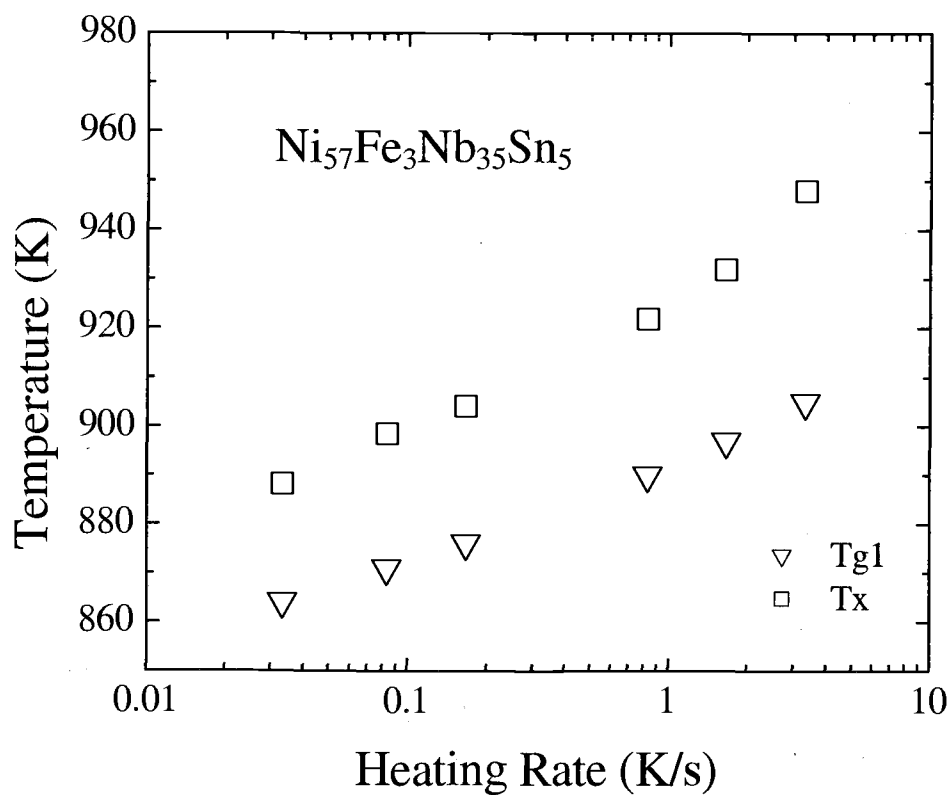


Figure 13: Onsets of glass transition temperature, T_{g1} , and crystallization temperature, T_x , from the continuous heating curves for $Ni_{57}Fe_3Nb_{35}Sn_5$

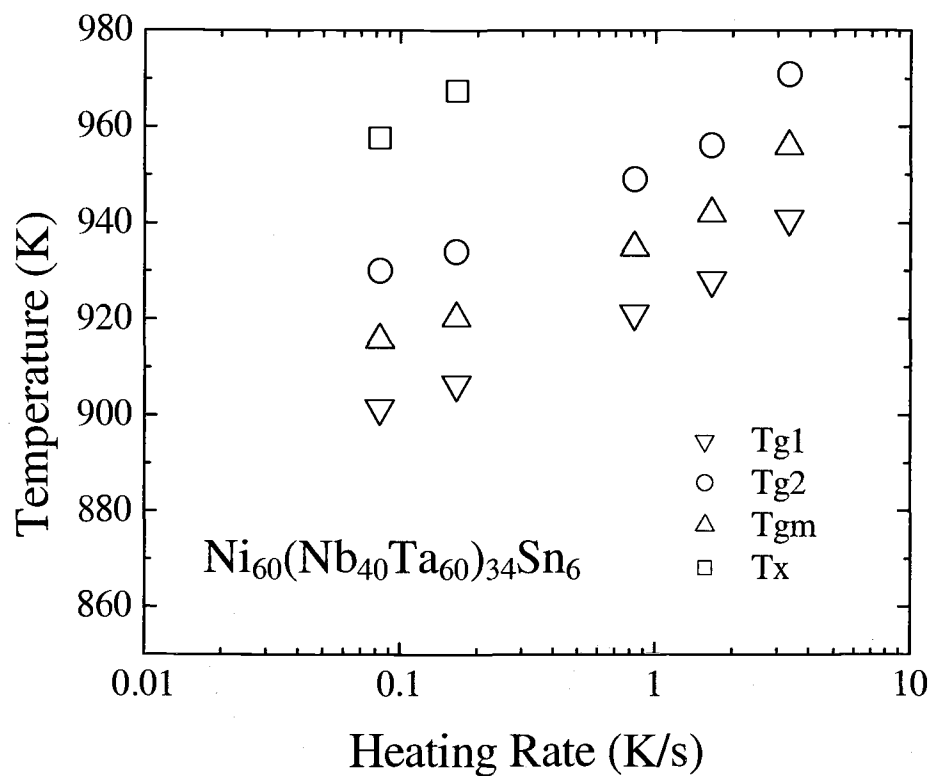


Figure 14: Onsets of glass transition temperature, Tg1, crystallization temperature Tx, the end glass transition temperature, Tg2, and the temperature midway between Tg1 and Tg2, Tgm, from the continuous heating curves for



Figures 15 to 21 show the continuous heating curves for the Vit1 series alloys. It can be seen in Figs. 15 to 21 that for the Vit1 series the change in T_g for changing heating rate is smallest for the Vit4 alloy and is largest for the Vit1(-b) alloy. The heating rate dependence of the glass transition temperature increases monotonically with the gradual change between the compositions between Vit4 and Vit1(-b).

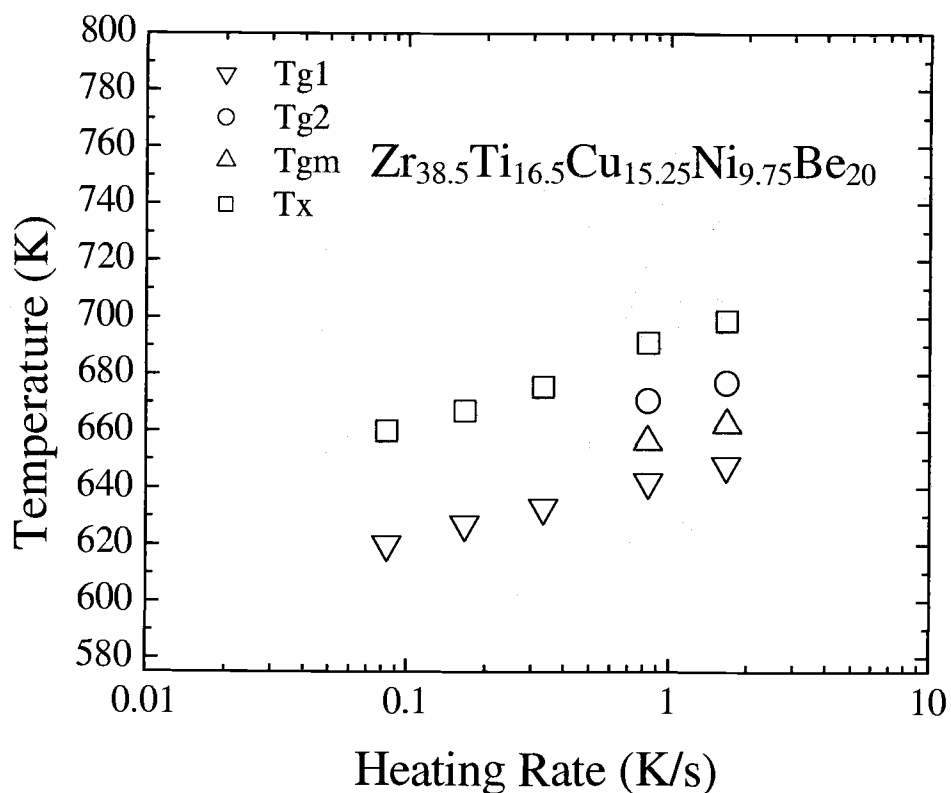


Figure 15: Onsets of glass transition temperature, T_{g1} , crystallization temperature T_x , the end glass transition temperature, T_{g2} , and the temperature midway between T_{g1} and T_{g2} , T_{gm} , from the continuous heating curves for Vit1(-b)

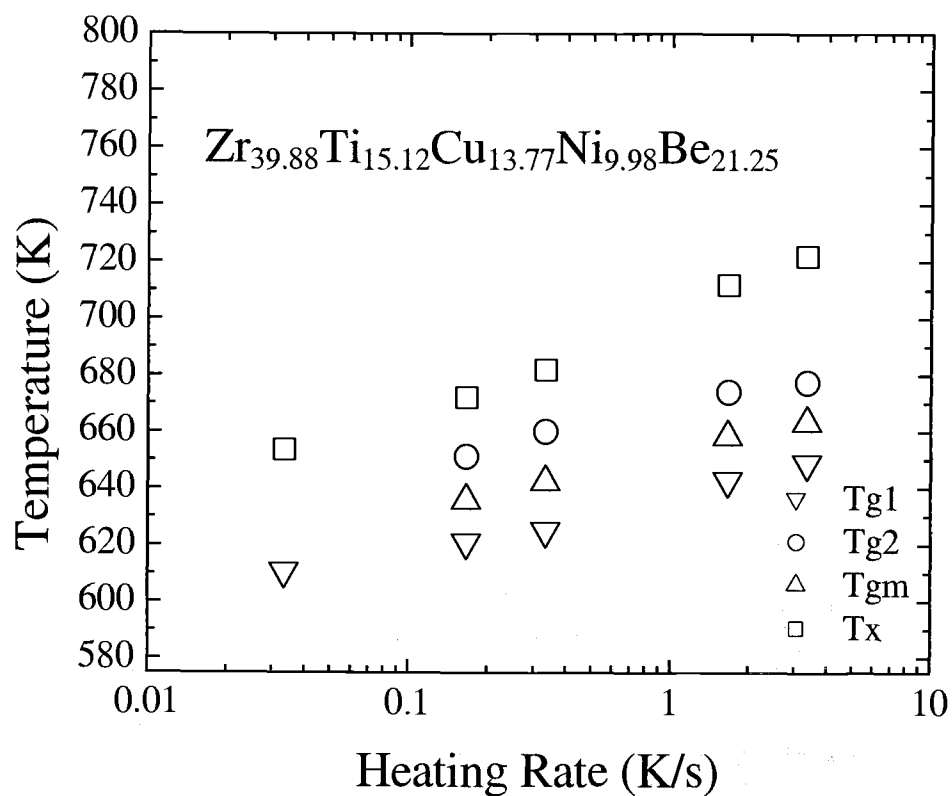


Figure 16: Onsets of glass transition temperature, Tg1, crystallization temperature Tx, the end glass transition temperature, Tg2, and the temperature midway between Tg1 and Tg2, Tgm, from the continuous heating curves for Vit1(-a)

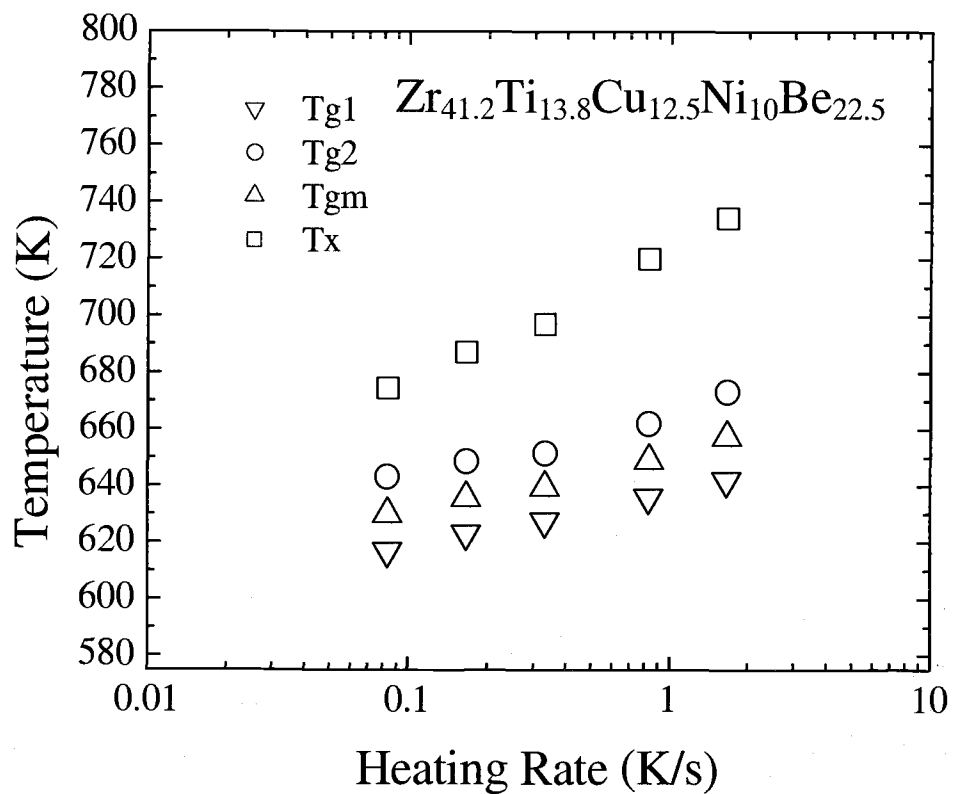


Figure 17: Onsets of glass transition temperature, Tg1, crystallization temperature Tx, the end glass transition temperature, Tg2, and the temperature midway between Tg1 and Tg2, Tgm, from the continuous heating curves for Vit1

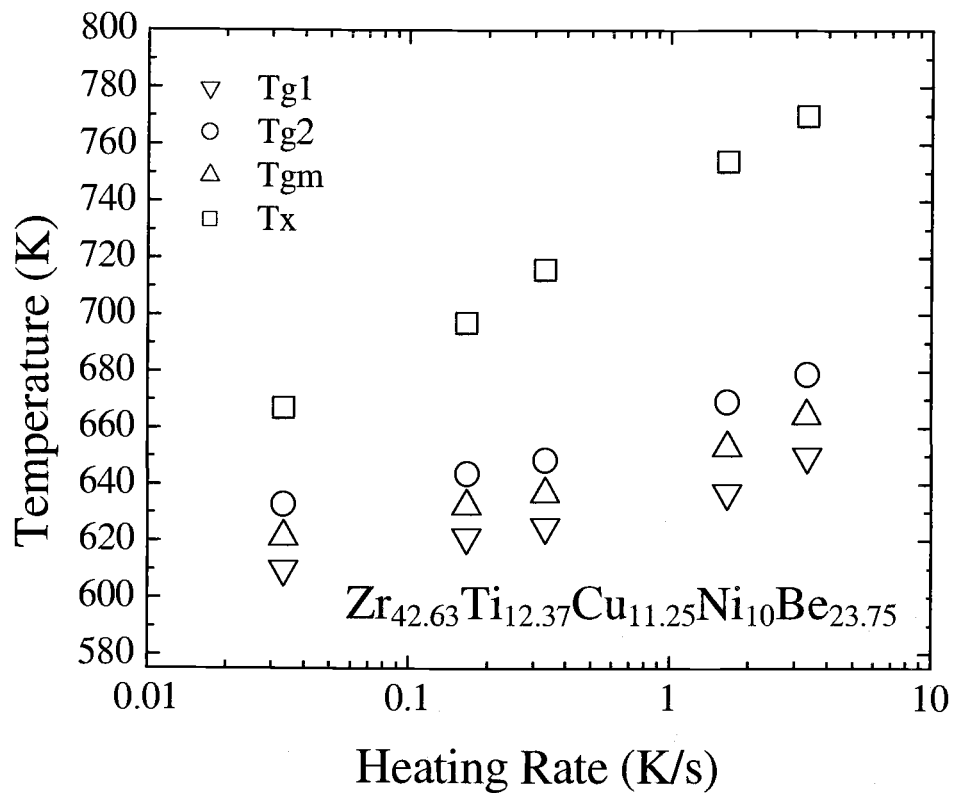


Figure 18: Onsets of glass transition temperature, T_{g1} , crystallization temperature T_x , the end glass transition temperature, T_{g2} , and the temperature midway between T_{g1} and T_{g2} , T_{gm} , from the continuous heating curves for Vit1a

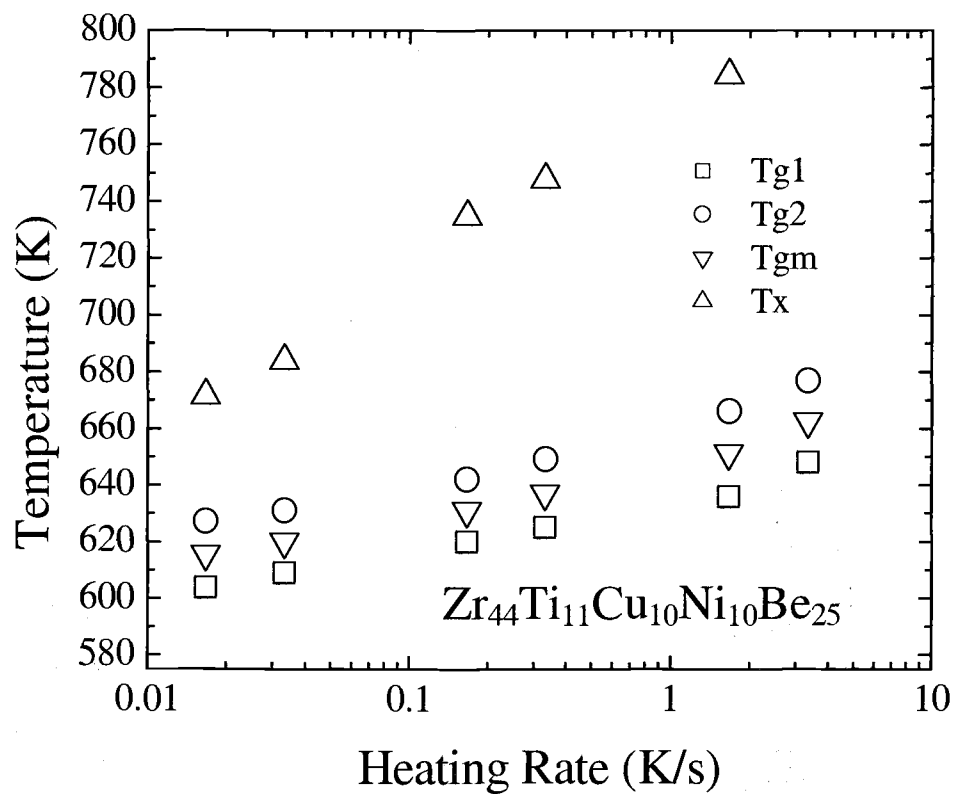


Figure 19: Onsets of glass transition temperature, Tg1, crystallization temperature Tx, the end glass transition temperature, Tg2, and the temperature midway between Tg1 and Tg2, Tgm, from the continuous heating curves for Vit1b

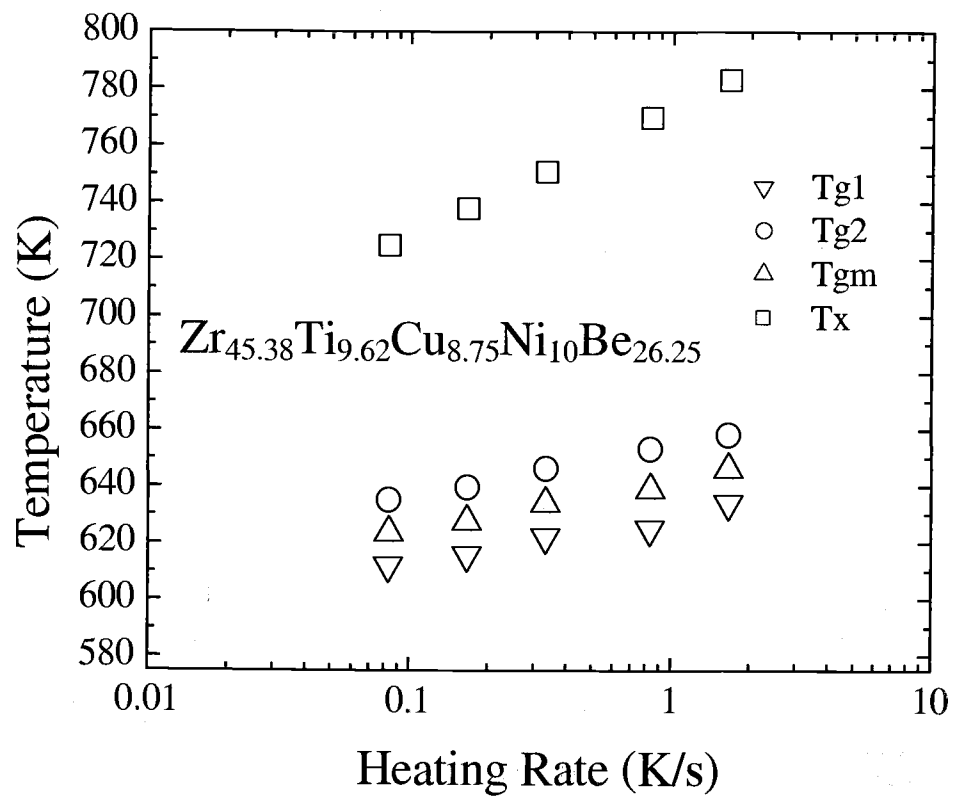


Figure 20: Onsets of glass transition temperature, Tg1, crystallization temperature Tx, the end glass transition temperature, Tg2, and the temperature midway between Tg1 and Tg2, Tgm, from the continuous heating curves for

Vitlc

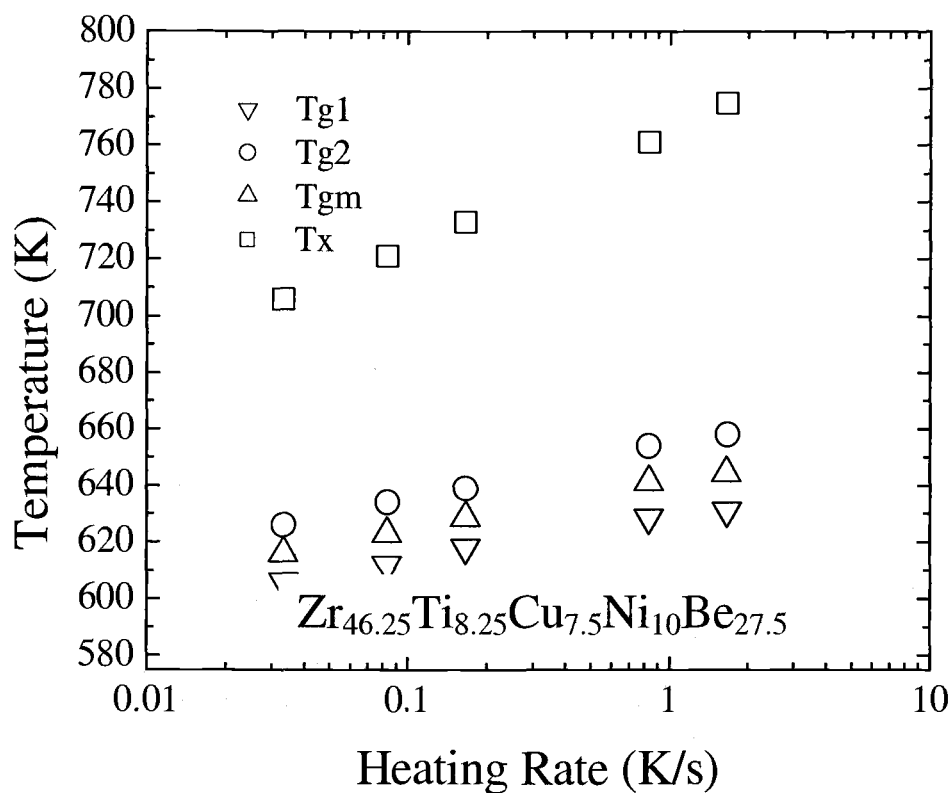


Figure 21: Onsets of glass transition temperature, Tg1, crystallization temperature Tx, the end glass transition temperature, Tg2, and the temperature midway between Tg1 and Tg2, Tgm, from the continuous heating curves for Vit4

4.1.3 Temperature Dependence of Structural Relaxation Time

For metallic glasses structural relaxation corresponds to specific heat capacity relaxation so structural relaxation can be calorimetrically observed in the temperature interval²⁶, ΔT_g . ΔT_g is defined as the range of temperatures between the onset and the end of the endothermic heat event that is characteristic of the glass transition and illustrated in Fig. 1¹. At a constant heating rate in the DSC a particular range of temperatures corresponds to a particular time interval. Therefore, the heating rate is related to the structural relaxation time, τ , with

$$\tau = \Delta T_g / R \quad (6)$$

where R is the heating rate²⁶ in the DSC. The T_g observed at the heating rate used in Eq. 6 represents the temperature that corresponds to that relaxation time. Figure 22 and 23 show the relaxation time as approximated by Eq. 6 versus temperature for the Nb-Ni based alloys and the Vit1 series alloy respectively. Since ΔT_g is nearly constant at different heating rates for all the alloys in this study, the inverse heating rate can also be used to represent τ when analyzing temperature dependence.

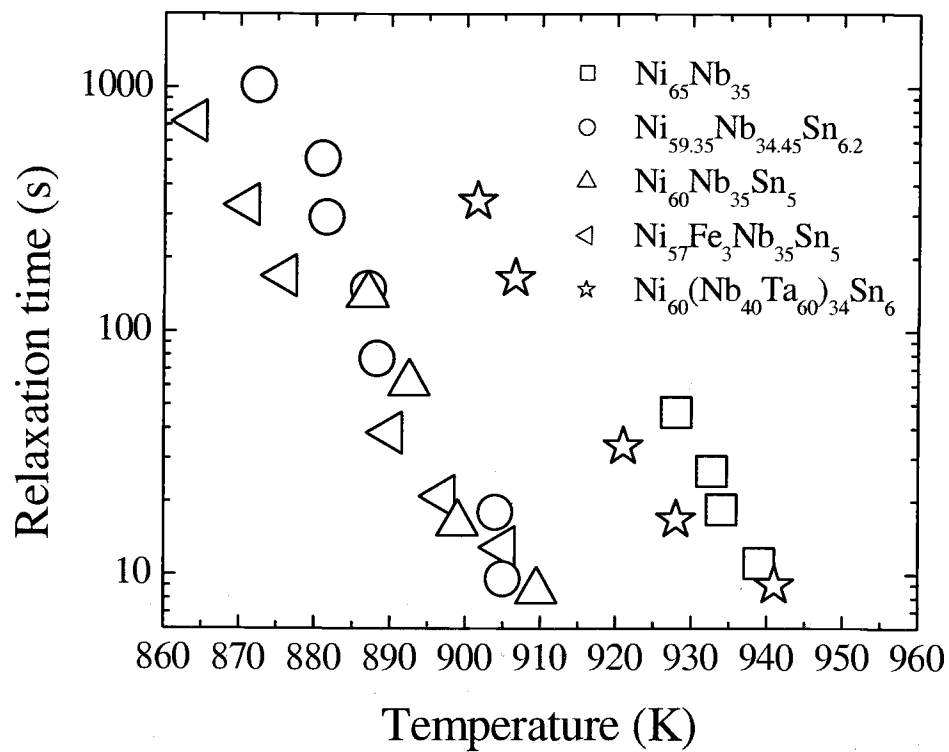


Figure 22: Relaxation time versus temperature for all the Nb-Ni based alloys studied.

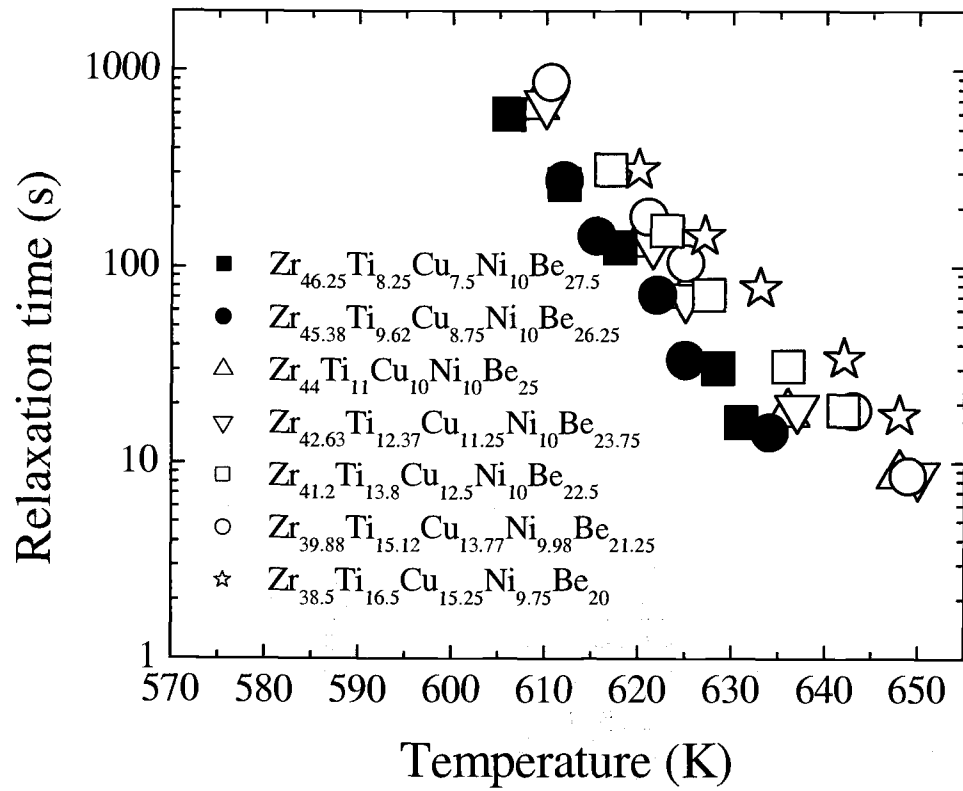


Figure 23: Relaxation time versus temperature for all the Vit1 series alloys studied.

4.1.4 Fit to the VFT Relation

Three parameters are used to quantify the fragility of glass forming materials. The first of those parameters is the steepness index, which is the slope m ^{27, 28},

$$m = \left. \frac{d \log_{10} \tau(T)}{dT_g / T} \right|_{T=T_g} \quad (7)$$

Where τ is the viscosity, T_g is the onset glass transition temperature, and T is the temperature. This is the slope of the curve on a plot that is similar to the Angell plot shown in Fig 2 at the glass transition temperature. For strong glass formers $m > 30$ is found with a lower limit of ≈ 14 . For example SiO_2 has an $m = 20$ ²⁹. For fragile glass formers one finds $m \geq 100$. For example polyvinyl chloride has an $m = 191$ ³⁰. Bulk metallic glasses are thought to be intermediate between these glass formers with steepness indices between those of fragile and strong glass formers, for instance $\text{Ge}_{3.3}\text{As}_{3.3}\text{Se}_{93.4}$ is an intermediate glass former with $m = 76$ ³¹.

The temperature dependence of the relaxation time for glass forming materials can be described by the Vogel-Fulcher-Tammann (VFT) relation³²

$$\tau = \tau_0 \exp\left(\frac{D^* \cdot T_0}{T - T_0}\right) \quad (8)$$

In this formula D^* is the fragility parameter and T_0 is the VFT temperature, which is defined as the temperature at which the kinetic resistance to flow approaches infinity. D^* is the second and T_0 is the third parameter which is

used to quantify the fragility of glass forming materials. Strong glass formers have $D^* \approx 100$ and fragile glass formers have $D^* \approx 5$. Intermediate glass formers have a range of D^* from about 10 to about 50. Materials with higher values of D^* have smaller values for T_0 , furthermore materials with higher values of D^* have smaller values for m . The inverse heating rate from Eq. 6 can be used to substitute τ in Eq. 8. The resulting relation between R and T were fit to the experimental data to find D^* and T_0 for the alloys in this study. Values of m were determined by calculating the derivatives of the best fits at $T_g^*/T = 1$. The results of the best fits of the data for each alloy are summarized in Table I.

Table I: The VFT parameters that result from the best fit of the VFT relation to the data.

Alloy	D^*	T_0 (K)	m
$\text{Ni}_{65}\text{Nb}_{35}$	6.2	784	110
$\text{Ni}_{60}\text{Nb}_{35}\text{Sn}_5$	11.0	670	70
$\text{Ni}_{59.35}\text{Nb}_{34.45}\text{Sn}_{6.2}$	11.0	670	70
$\text{Ni}_{60}(\text{Nb}_{40}\text{Ta}_{60})_{34}\text{Sn}_6$	15.7	620	52
$\text{Ni}_{57}\text{Fe}_3\text{Nb}_{35}\text{Sn}_5$	16.4	591	50
$\text{Zr}_{46.75}\text{Ti}_{8.25}\text{Cu}_{7.5}\text{Ni}_{10}\text{Be}_{27.5}$ (Vit 4)	19.1	395	46
$\text{Zr}_{45.38}\text{Ti}_{9.62}\text{Cu}_{8.75}\text{Ni}_{10}\text{Be}_{26.25}$ (Vit 1c)	20.6	384	44
$\text{Zr}_{44}\text{Ti}_{11}\text{Cu}_{10}\text{Ni}_{10}\text{Be}_{25}$ (Vit 1b)	24.6	360	39

$Zr_{42.63}Ti_{12.37}Cu_{11.25}Ni_{10}Be_{23.75}$ (Vit 1a)	25.7	354	38.1
$Zr_{41.2}Ti_{13.8}Cu_{12.5}Ni_{10}Be_{22.5}$ (Vit1)	25.8	354	37.9
$Zr_{39.88}Ti_{15.12}Cu_{13.77}Ni_{9.98}Be_{21.25}$ (Vit -a)	27.6	343	36.5
$Zr_{38.5}Ti_{16.5}Cu_{15.25}Ni_{9.75}Be_{20}$ (Vit -b)	31.9	324	33.7

4.2 Study on the Equilibrium Phases of Vit106

In this investigation we determine the crystalline equilibrium phases of Vit106. By comparing the composition of the equilibrium phases to the nominal composition of the melt it is possible to map the redistribution of the elements during crystallization, thereby observing the effect of the liquid composition on the crystallization kinetics of the alloy. This portion of the study gives qualitative insight into some of the effects of composition and diffusivity on GFA in the context of the hard sphere model.

4.2.1 Backscatter Image of Vit 106

The backscattering image of the Vit 106 microstructure is depicted in Fig. 24. The length scale of the features in the microstructure of the Vit 106 sample, shown in Fig. 24, ranges from 10 to 50 μm . Such a large size implies that the crystallization kinetics are relatively fast in Vit 106. The contrast in images collected by backscattering electrons is caused by either the topography of the sample or the variations in atomic number within the sample³³. The topography of this sample was minimized by polishing, so the difference in gray scales represents the difference in composition, and therefore the different phases in the microstructure. In order to determine the compositions, the electron beam was focused at many locations on the sample. The same procedures were performed on a similar alloy $\text{Zr}_{58.5}\text{Cu}_{15.6}\text{Ni}_{12.8}\text{Al}_{10.3}\text{Nb}_{2.8}$ (Vit 106a), but its crystal size was much smaller than the crystal size of Vit 106 and below the resolution of the electron beam. Hence the results of the EMPA on Vit 106a were inconclusive. However the length scale difference in the microstructure indicates that Vit 106a has more sluggish crystallization kinetics than Vit 106 and therefore has a better glass forming ability. This has been suggested previously³⁴.

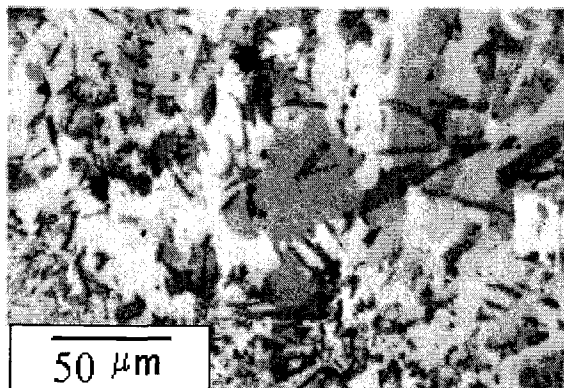


Figure 24: Backscattering image of slowly cooled Vit 106. The length scales of the phases in Vit 106 vary between 10 and 50 μm . The different gray scales represent different compositions.

4.2.2 Vit 106 Composition Analysis

To collect data that was representative of the entire sample, the electron beam traversed the sample surfaces in three lines that were spaced evenly. Selected area analysis was performed in areas with different gray levels. The electron microprobe scans were organized into compositional profiles. Figure 25 shows the cumulative concentrations plotted versus the Al concentration of compositional readings at 143 locations. Some general trends can be noticed in Fig. 25. The concentration of Zr, Cu, and Ni decrease as the concentration of Al increases. This suggests that Al replaces Cu and Ni in the crystal structures. On the other hand the concentration of Nb increases with

increasing Al concentration, suggesting that Nb replaces Zr in the crystal structures.

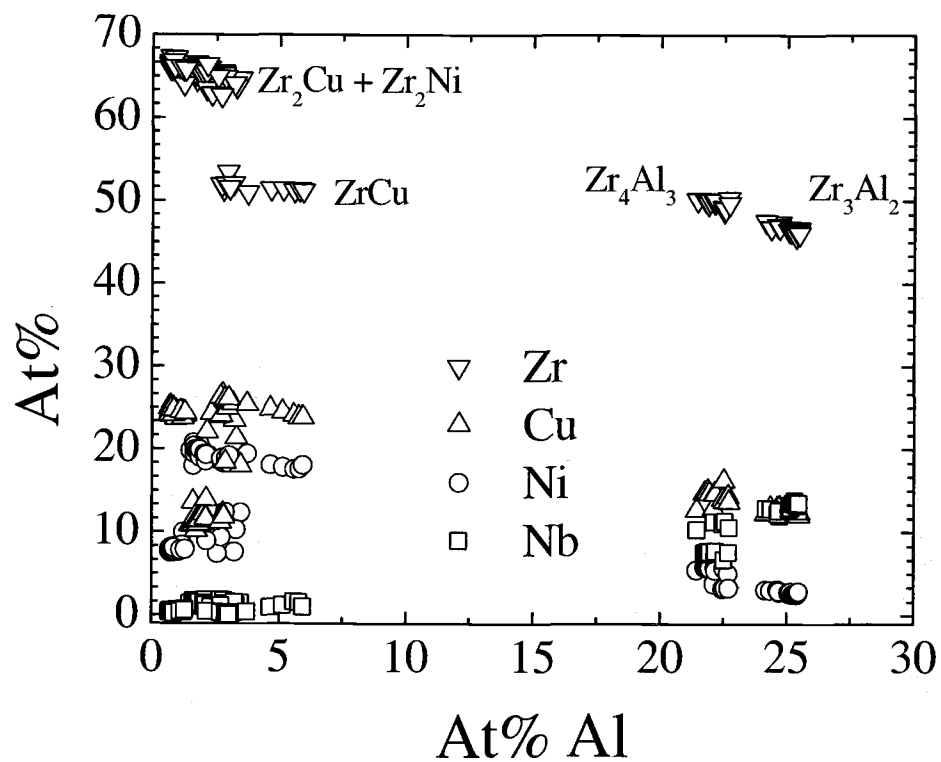


Figure 25: Example of a plot where the compositions of four components of Vit 106 are plotted against the fifth. This type of plot is used for cluster analysis. The compositions of Zr (∇), Cu (\triangle), Ni (O), and Nb (\square) are all plotted against the composition of Al.

4.2.3 Equilibrium Phases based on Binary Phase Diagrams

In the data set there are five compositional categories that can be attributed to different phases³⁵. Compositional readings were grouped into these categories and tested with cluster analysis for distinctness. Readings that did not fit into distinct clusters were removed. The readings that did not fit were likely the compositional average of more than one phase. Compositional averaging occurs when the electron beam is focused on a region that contains more than one phase. If we consider the atomic sizes, we can make predictions about which element can substitute another element in the crystal structure. For instance Nb ($r = 0.208$ nm) and Zr ($r = 0.216$ nm) are likely to occupy the same locations in a crystal structure, and that Cu ($r = 0.157$ nm), Ni ($r = 0.162$ nm), and to some degree Al ($r = 0.182$ nm) can substitute each other in the same crystal structures. The average compositions of the different phases are summarized and compared with the nominal composition of the melt in Table II. The first phase has a lower concentration of Nb and Al, and a higher concentration of Ni and Zr than amorphous Vit 106. Its average composition is $Zr_{65.6}Cu_{11.5}Ni_{19.4}Al_{2.0}Nb_{1.5}$. This composition is likely to have a Zr_2Ni crystal structure because it contains two thirds of Zr and the rest is rich in Ni. Only traces of Al and Nb are found in this phase. The second phase is similar to the first in that it has a very low concentration of Nb and Al, and a higher concentration of Zr than amorphous Vit 106. However, instead of having a high concentration of Ni it has a high concentration of Cu. Its average

composition is $Zr_{66.1}Cu_{24.3}Ni_{8.0}Al_{1.1}Nb_{0.5}$, and this composition is likely to have a Zr_2Cu crystal structure. The third phase has a lower concentration of Zr, Al, and Nb, and it has a higher concentration of Cu compared to the Vit 106 melt. Its average composition is $Zr_{51.7}Cu_{25.1}Ni_{18.5}Al_{4.0}Nb_{0.7}$, and this composition is likely to have a $ZrCu$ crystal structure. The fourth phase has a lower concentration of Zr, Cu, and Ni, and a higher concentration of Al and Nb. Its average composition is $Zr_{47.3}Cu_{12.4}Ni_{2.7}Al_{24.9}Nb_{12.7}$. This composition is likely to have a Zr_3Al_2 crystal structure as has been suggested in other work³⁶. The sum of the concentrations of Zr and Nb add to about 60%, which suggests that Nb substitutes Zr in the crystal structure. The fifth phase is similar in the composition to the fourth but it has a lower concentration of Nb and Al and a higher concentration of Zr, Cu, and Ni. Its average composition is $Zr_{50}Cu_{14.6}Ni_{5.3}Al_{22.0}Nb_{8.1}$. Its total amount of Zr plus Nb is 58.1 at%. This suggests that it consists of the Zr_4Al_3 crystal structure in which Nb substitutes Zr and Cu and Ni substitute Al³⁵.

4.2.4 Vit 106 X-ray Diffraction Profile

X-ray diffraction (XRD) was performed on the sample. The XRD pattern for crystallized Vit 106 is shown in Fig. 26. The intensities are shown as a function of 2θ . For Vit 106, all dominant peaks or overlapping peaks could be attributed to one of the five following structures: Zr_2Ni ³⁷, Zr_2Cu ³⁸, $ZrCu$ ³⁹,

Zr_3Al_2 ³⁷, and Zr_4Al_3 ⁴⁰. The matching peaks in Fig. 26 are labeled with different symbols for each structure. Table II summarizes these results.

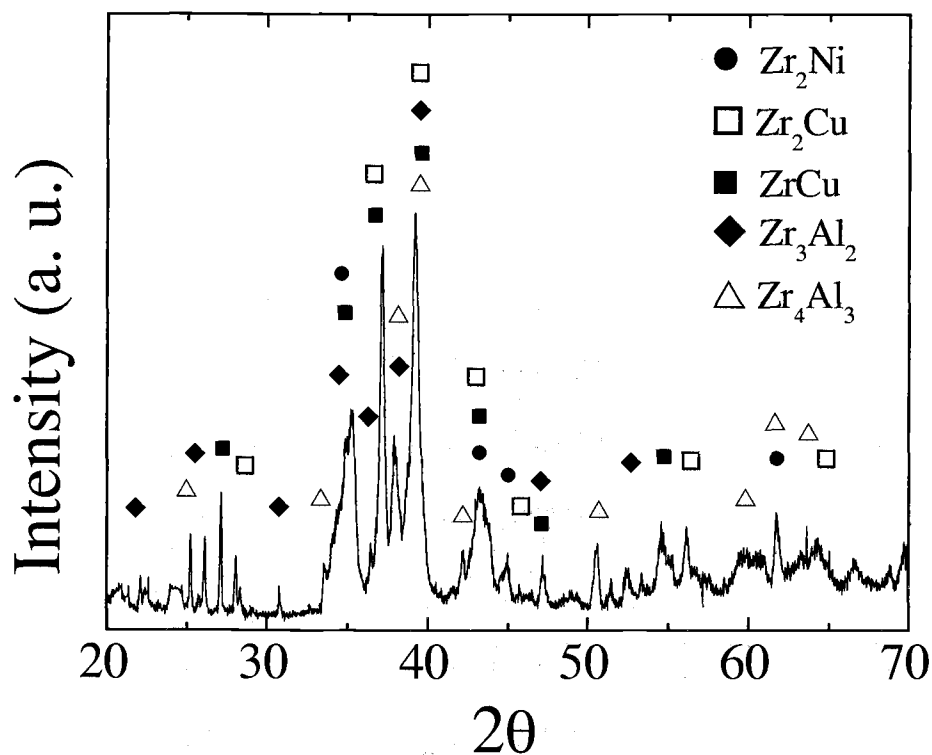


Figure 26: X-ray diffraction pattern for crystallized Vit 106. The peaks that represent the Zr_2Ni (●), Zr_2Cu (□), $ZrCu$ (■), Zr_3Al_2 (◆), and Zr_4Al_3 (△) crystal structures are labeled accordingly.

Table II: Composition of the phases and their corresponding crystal structure.

Composition	Zr (at%)	Cu (at%)	Ni (at%)	Al (at%)	Nb (at%)	Crystal Structure
Nominal	57	15.4	12.6	10	5	Glass
1	65.6	11.5	19.4	2.0	1.5	Zr ₂ Ni
2	66.1	24.3	8.0	1.1	0.5	Zr ₂ Cu
3	51.7	25.1	18.5	4.0	0.7	ZrCu
4	47.3	12.4	2.7	24.9	12.7	Zr ₃ Al ₂
5	50.0	14.6	5.3	22.0	8.1	Zr ₄ Al ₃

5. DISCUSSION

5.1 The Supercooled Liquid Region for the Vit 1 Series and Vit 4

It can be seen in Fig. 9 that ΔT was smallest for Vit1(-b), larger for Vit 1, and the largest for Vit 4. This represents a reduction in the supercooled liquid region for these alloys with increased concentration of Ti and Cu and decreased concentration of Zr and Be. This trend has been observed by others⁴¹, and is consistent with the intermediate alloys in the system.

5.2 Heating Rate Dependence of T_g

Small heating rate dependence of T_g indicates a fragile glass, whereas large heating rate dependence is characteristic of a strong glass. Figures 10 to 12 demonstrate that the $Ni_{60}Nb_{35}Sn_5$ and $Ni_{59.35}Nb_{34.45}Sn_{6.2}$ alloys are stronger glass formers than the $Ni_{65}Nb_{35}$ alloy because their T_g decreases more rapidly with decreasing heating rate. Likewise Figs. 10 to 14 demonstrate that the $Ni_{60}(Nb_{40}Ta_{60})_{34}Sn_6$ and $Ni_{157}Fe_3Nb_{35}Sn_5$ alloys are stronger glass formers than either the $Ni_{60}Nb_{35}Sn_5$ or $Ni_{59.35}Nb_{34.45}Sn_{6.2}$ alloys because their T_g decreases more rapidly with decreasing heating rate. This is confirmed by the fragility parameters shown in Table I.

Figures 15 to 21 show that the heating rate dependence of T_g increases from Vit4 to Vit1(-b), and that this trend is consistent with the intermediate alloys of the system. It is expected that the Vit1(-b) is the strongest glass former in the system, and that the alloys become incrementally more fragile in the intermediate alloys with the most fragile alloy being Vit 4. This is confirmed by the fragility parameters shown in Table I. It is important to recognize that ΔT is smallest for the strongest alloy and that ΔT is largest for the most fragile alloy.

5.3 Fragility Plots

The fragility plot for the Nb-Ni based alloys is shown in Fig. 27. In this plot the inverse heating rate is plotted as a function of inverse temperature normalized to T_g^* . T_g^* is the onset temperature of the glass transition measured at a heating rate 0.0167 Ks^{-1} in the DSC. The data were fit to the VFT-type Eq. 8 using the inverse heating rate from Eq. 6 to approximate τ . τ_0 was held constant at 10^{-14} sK^{-1} because that heating rate is approximately proportional to the relaxation time to which all materials tend at infinite temperature. The resulting fits are plotted as lines in Fig. 27. The Nb-Ni based alloys fit intermediate between o-terphenyl and SiO_2 in a fragility plot, with strong liquid behavior increasing as the number of components in the alloy increases.

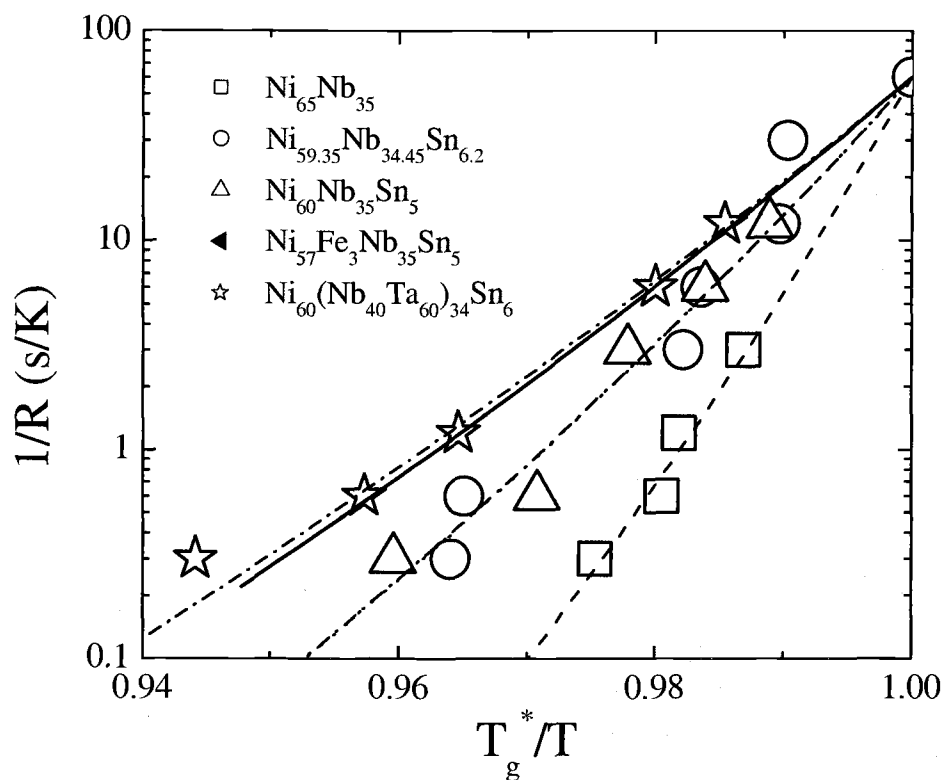


Figure 27: Fragility plot comparing the five Nb-Ni alloys studied.

Figure 28 shows the fragility plot for the Vit1 series alloys, Vit4 is included on the plot for comparison. The fragilities of the Vit 1 series alloys are more similar to each other than the fragilities of the Nb-Ni based alloys are, so Fig 28 is reproduced in Fig 29 on a smaller scale.

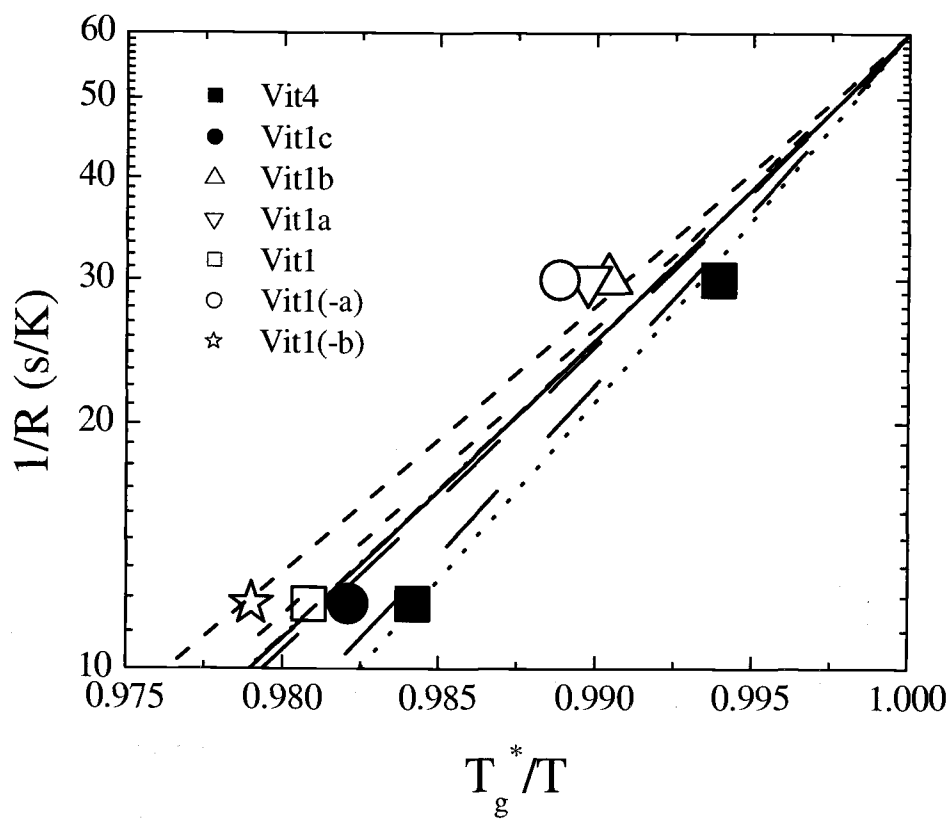


Figure 29: Enhanced view of Fig. 28. Fragility plot comparing the seven Vit1 series alloys studied.

5.4 The Effect of Increasing Complexity on D^*

Alloys that involve a combination of early and late transition metals in a dense arrangement of atoms at the melting temperature exhibit strong liquid behavior. On the other hand, alloys that have a looser arrangement of atoms at the melting temperature tend to exhibit fragile liquid behavior. For kinetic and thermodynamic reasons, denser liquids tend to have better glass forming ability (GFA). This suggests that alloys that show strong liquid behavior will tend to have higher GFA than alloys that show fragile liquid behavior. In this way the fragility of an alloy seems to relate to its GFA.

For the Nb-Ni based alloys D^* increases linearly as the number of components in the alloy increases. This relationship is shown in Fig. 30. Extrapolation of the trend shown in Fig. 30 down to a one component system yields $D^* \approx 2$, which is in good agreement with the estimated fragility of pure metals using their melt viscosity and apparent activation energies for flow. The fragility parameters of the Nb-Ni alloys are compared with the fragility parameters of other metallic glass forming alloys in Fig. 31. The increase of the fragility parameter with the number of components in Nb-Ni based alloys is also observed in Zr – based alloys. It reflects the slowdown in kinetics and thus the increase in glass forming ability with the increase of the number of components. That the fragilities are slightly different for the quaternary alloys however suggests that not only the number of components in an alloy but also

the type of elements in an alloy with the same number of components affect the fragility of the alloy.

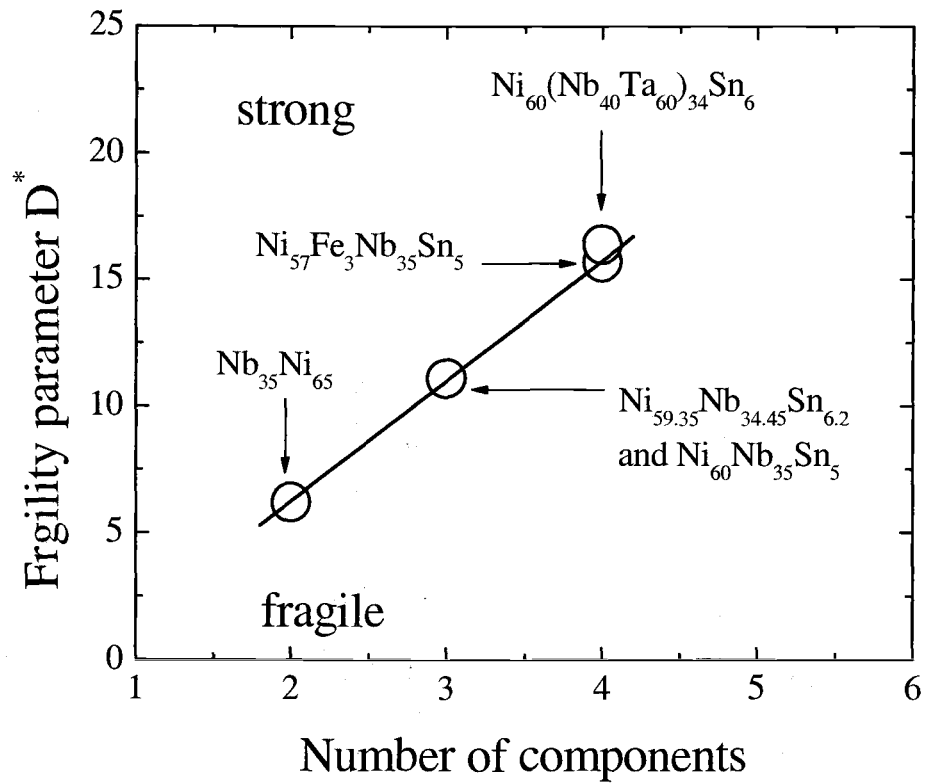


Figure 30: Fragility parameter for the Nb-Ni based system plotted versus the number of components in the alloy.

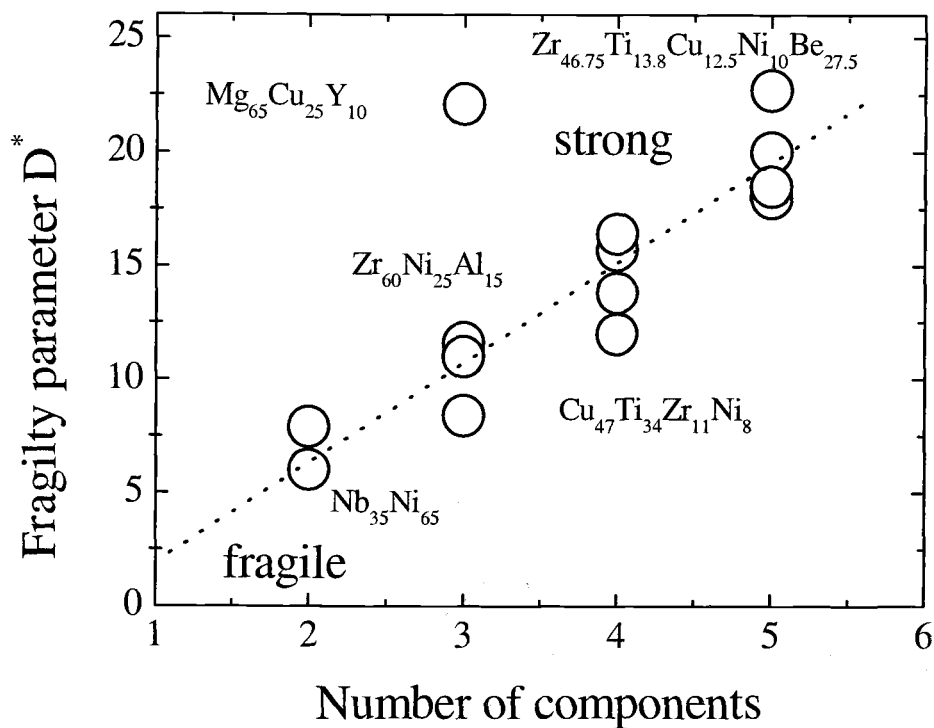


Figure 31: Fragility parameter plotted versus the number of components in the alloy. The Nb-Ni based system is compared to other glass forming systems.

This suggests that it is possible to increase the density of a liquid by selectively replacing the elements of the alloy system with other elements. For instance the replacement of Ni ($r = 0.162$ nm) in Nb₃₅Ni₆₅ by Sn ($r = 0.172$ nm) yields Ni₆₀Nb₃₅Sn₅. The ternary alloy will be more closely packed because the three different size atoms can fill space more efficiently. To ensure that the addition of Sn does not decrease the density of the liquid, sufficient amounts of Ni and Nb ($r = 0.208$ nm) remain. The additional replacement of Ni by Fe ($r = 0.172$) in the Ni₅₇Fe₃Nb₃₅Sn₅ alloy enhances this

effect, and therefore this quaternary alloy is denser than its ternary counterpart. Increasing the number of components in a system develops size mismatch. On the other hand the replacement of Nb by Ta ($r = 0.209$ nm) in $Ni_{60}(Nb_{40}Ta_{60})_{34}Sn_6$ causes the quaternary alloy to be denser than its ternary counterpart because Ta is heavier than Nb, although the elements are the same size.

5.5 The Effect of Concentration on D*

For the Vit1 series and Vit4, D^* increases with increasing concentration of Ti and Cu. Likewise D^* increases with decreasing concentration of Zr and Be. These trends are shown in Figs. 32 to 35. The fragilities for the Vit1 series and Vit4, shown in Table I, vary between 19 and 32. This wide range of D^* suggests that, for complex glass forming systems with the same number and type of components, the concentration of the components has a significant effect on the structural stability of the system. This indicates that designing dense alloys involves optimizing the concentration of the elements as well as developing a size mismatch between components.

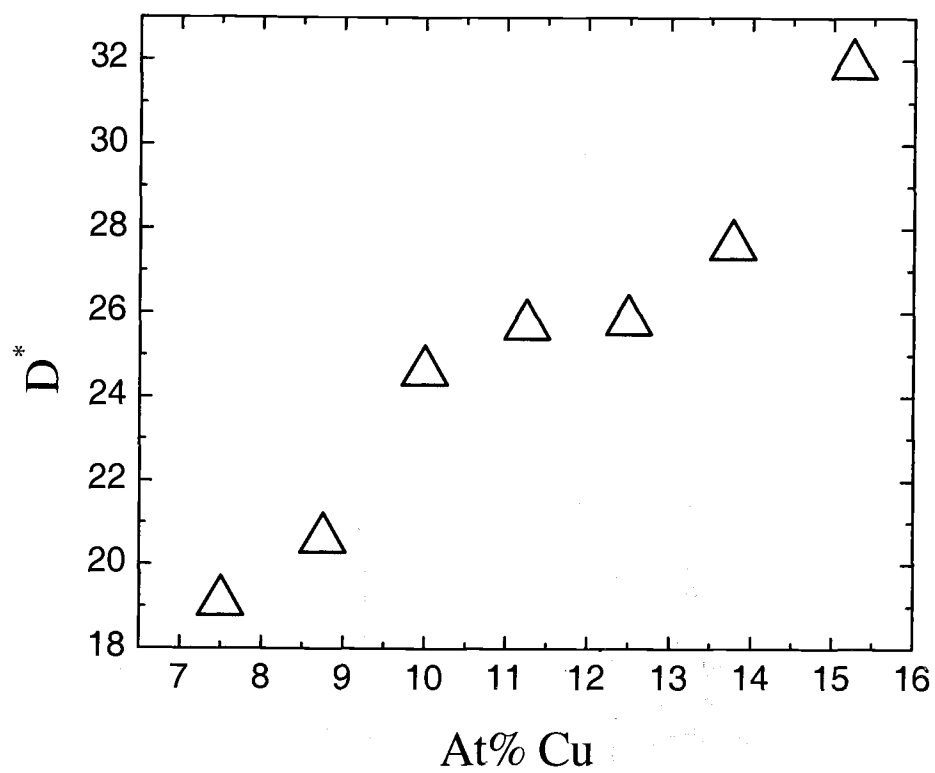


Figure 32: Fragility parameter D^* plotted versus the concentration of Cu in the glass forming alloy.

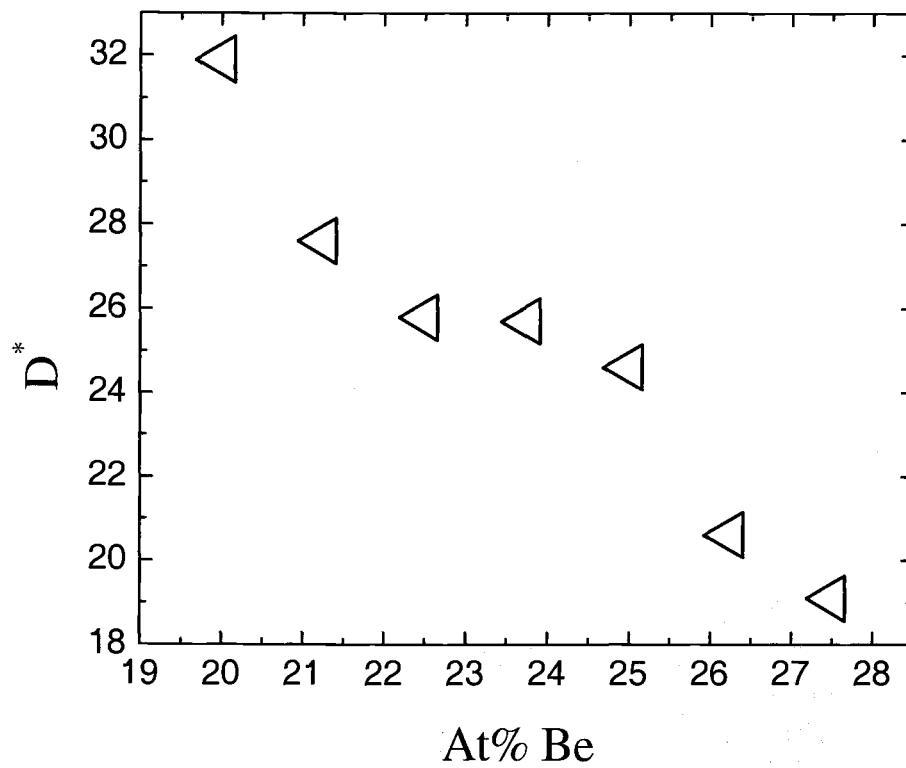


Figure 33: Fragility parameter D^* plotted versus the concentration of Be in the glass forming alloy.

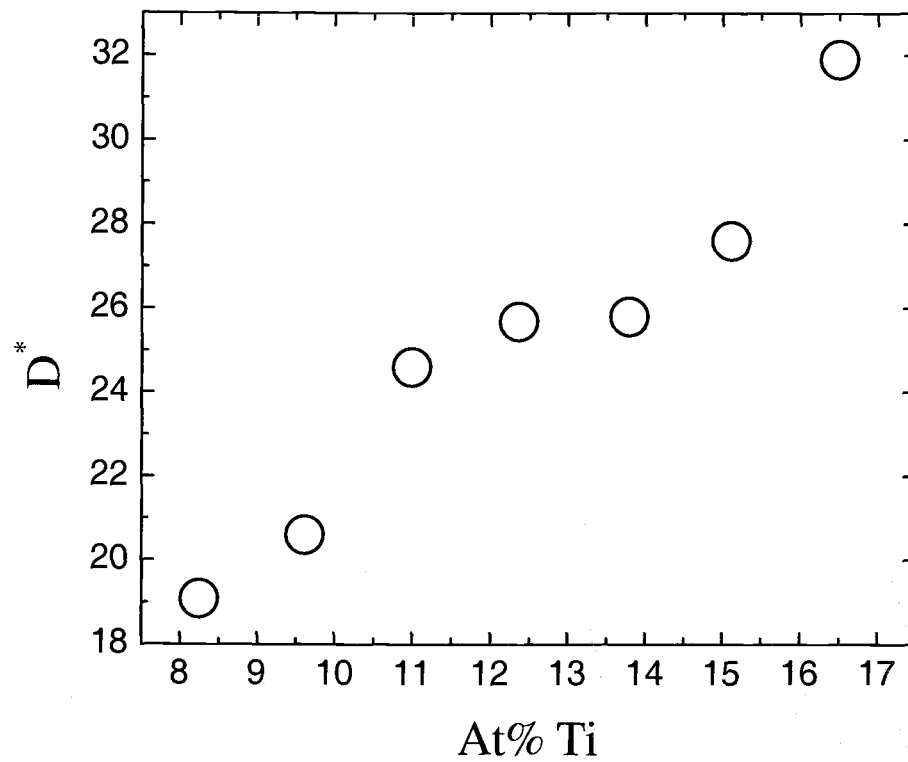


Figure 34: Fragility parameter D^* plotted versus the concentration of Ti in the glass forming alloy.

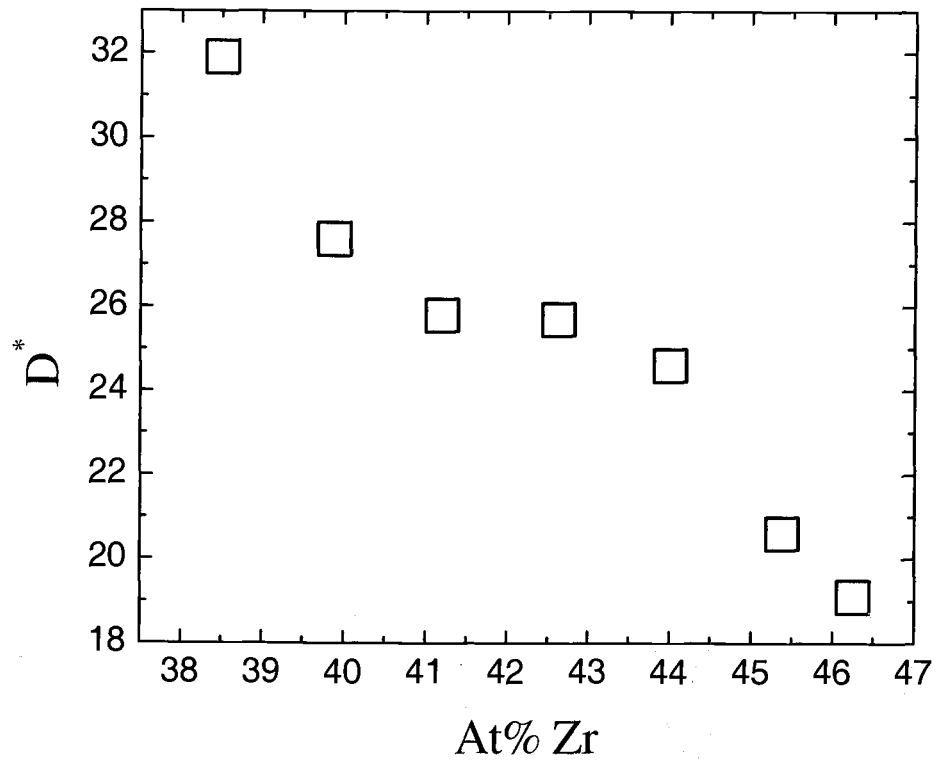


Figure 35: Fragility parameter D^* plotted versus the concentration of Zr in the glass forming alloy.

5.6 Crystal Structure Solubility in Vit 106

All the equilibrium phases of Vit 106 contain the respective other elements as solutes in their crystal structures. The Zr_2Cu and the Zr_2Ni phase contain only traces of Nb and Al. In the Zr_2Cu structure the Ni replaces about one quarter of the Cu and in the Zr_2Ni structure the Cu replaces about one third of the Ni. The $ZrCu$ phase contains only traces of Nb. Ni replaces about 40% of the Cu and Al about 10%. The Zr_3Al_2 and Zr_4Al_3 are enriched in Nb compared to the nominal Nb concentration. The Zr and the Nb add to about 60% in both Al rich phases. Cu and Ni substitute about half of the Al.

5.7 Diffusion of Al and Nb in Vit 106

It is especially interesting to compare the nominal compositions of the Nb and the Al with the composition of these elements in the different crystalline equilibrium compounds. Table II shows the equilibrium concentrations of Nb in each phase. Nb is the second largest atom in the alloy and likely the second slowest moving species after Zr. The first three phases in Table II are depleted to about 1% Nb and the last two phases are enriched far beyond the nominal composition of Nb in the alloy. This means a considerable concentration redistribution of Nb in or out of certain regions has to occur to nucleate and grow any of the five phases. If we decrease the Nb concentration in the melt,

the Zr_2Ni , Zr_2Cu , and $ZrCu$ formation would be more favored because the alloy is already depleted of Nb. If we would increase the nominal Nb concentration of the melt, formation of the Zr_3Al_2 and Zr_4Al_3 phases might become more favorable, since Nb can substitute Zr. From the viewpoint of how much concentration redistribution of Nb is necessary to form a nucleus, the composition of 5 at% is beneficial not to favor either the Nb-rich or Nb-poor phases. A similar pattern is found for Al. As can be seen in Table 4.II, Zr_3Al_2 and Zr_4Al_3 are rich in Al, the other phases are depleted of Al. The nominal Al composition of the melt of 10 at% is balanced in between the Al poor and Al enriched phases. Hence, both Nb and Al have to diffuse out of areas, where Zr_2Ni , Zr_2Cu , or $ZrCu$ form. In turn, both Nb and Al need to diffuse into area where Zr_3Al_2 or Zr_4Al_3 form. In Zr_3Al_2 and Zr_4Al_3 , Al needs to get enriched, likely because the crystal structures can only accommodate Cu and Ni as a substitute for Al to a limited degree. The Nb is needed to substitute for Zr. Therefore, concentration redistribution of Al and Nb are mandatory for nucleation and growth of any of the equilibrium phases.

Similar trends can be observed, if we reduce the number of components and consider only the ternary Zr-Cu-Ni alloy system and the Zr_2Ni , Zr_2Cu , and $ZrCu$ phases. The addition of Cu to Zr-Ni or of Ni to Zr-Cu will retard the crystallization somewhat due to mandatory fluxes. However, Cu and Ni have approximately the same size and have faster diffusivities than Al and Nb, especially in the deeply undercooled melt when the diffusivities become

strongly size dependent⁴². Therefore substitution of Ni by Cu and vice versa is not very efficient and no bulk metallic glasses are formed in the Zr-Cu-Ni alloy system. However, if we substitute Cu or Ni by Al we get the best ternary Zr-based bulk metallic glasses. Those are in the Zr-Al-Ni and Zr-Al-Cu⁴³ systems, where the Al as the medium size atom acts in a similar way as in Vit106.

6. CONCLUSION

The heating rate dependence of the glass transition region and the crystallization of the $\text{Ni}_{65}\text{Nb}_{35}$, $\text{Ni}_{60}\text{Nb}_{35}\text{Sn}_5$, $\text{Ni}_{59.35}\text{Nb}_{34.45}\text{Sn}_{6.2}$, $\text{Ni}_{60}(\text{Nb}_{40}\text{Ta}_{60})_{34}\text{Sn}_6$, and $\text{Ni}_{57}\text{Fe}_3\text{Nb}_{35}\text{Sn}_5$ metallic glasses is investigated with differential scanning calorimetry. The fragilities of the alloys were characterized with the steepness index, m , the fragility parameter D^* , and the VFT temperature, T_0 which are the fit parameters from the VFT relation. It was found that the D^* increased with the number of components for the Nb-Ni metallic glass forming system studied. In particular it was found that the structural stability of Nb-Ni alloys with respect to temperature change can be improved by the addition of Sn. Furthermore it was found that the structural stability of Nb-Ni-Sn alloys with respect to temperature change can be improved with the addition of either Fe or Ta.

The Vit1 series alloys: $\text{Zr}_{45.38}\text{Ti}_{9.62}\text{Cu}_{8.75}\text{Ni}_{10}\text{Be}_{26.25}$ (Vit 1c), $\text{Zr}_{44}\text{Ti}_{11}\text{Cu}_{10}\text{Ni}_{10}\text{Be}_{25}$ (Vit1b), $\text{Zr}_{42.63}\text{Ti}_{12.37}\text{Cu}_{11.25}\text{Ni}_{10}\text{Be}_{23.75}$ (Vit1a), $\text{Zr}_{41.2}\text{Ti}_{13.8}\text{Cu}_{12.5}\text{Ni}_{10}\text{Be}_{22.5}$ (Vit1), $\text{Zr}_{39.88}\text{Ti}_{15.12}\text{Cu}_{13.77}\text{Ni}_{9.98}\text{Be}_{21.25}$ (Vit1(-a)), $\text{Zr}_{38.5}\text{Ti}_{16.5}\text{Cu}_{15.25}\text{Ni}_{9.75}\text{Be}_{20}$ (Vit1(-b)) bulk metallic glasses were also investigated with differential scanning calorimetry. $\text{Zr}_{46.75}\text{Ti}_{8.25}\text{Cu}_{7.5}\text{Ni}_{10}\text{Be}_{27.5}$ (Vit4) was included for comparison. It was found that D^* increases with

increasing concentration of Ti and Cu and decreasing concentration of Zr and Be.

Compositional and structural analysis of slowly cooled $Zr_{57}Cu_{15.4}Ni_{12.6}Al_{10}Nb_5$ (Vit106) was performed with an electron microprobe and by X-ray diffraction. Five different crystalline phases were detected that could all be derived from binary intermetallic compounds. The phases are Zr_2Ni , Zr_2Cu , $ZrCu$, Zr_3Al_2 , and Zr_4Al_3 . In every case the other three respective elements existed as solute in the phase. The analysis of the amount of solutes leads to the conclusion that, especially the particular compositions of Al and Nb play an important role in retarding the nucleation and growth kinetics. To nucleate and grow one of the five equilibrium phases a considerable concentration redistribution of both elements has to occur.

The fragility study of the Nb-Ni based and Vit1 series alloys suggests that a balance between size mismatch development and concentration of components can be reached to form a dense liquid with slow diffusivity. Alloys that are optimized in this way are likely to show good glass forming ability. The determination of the crystalline equilibrium phases of Vit 106 implies that an optimal concentration for a glass forming alloy frustrates crystallization by requiring considerable diffusion. This suggests that extremely dense metallic liquids that require vast redistribution of their elements in order to crystallize are ideal glass forming alloys.

7. BIBLIOGRAPHY

- ¹ A. Inoue, T. Zhang, and T. Masumoto, *Mater. Trans., JIM* **31**, 425 (1991).
- ² X. H. Lin and W. L. Johnson, *J. Appl. Phys.*, **78** 6514 (1995).
- ³ A. Peker and W. L. Johnson, *Appl. Phys. Lett.*, **63**, 2342 (1993).
- ⁴ T. Zhang, A. Inoue, and T. Masumoto, *Mater. Trans., JIM* **32**, 1005 (1991).
- ⁵ C. A. Angell, *Science* **267**, 1924 (1995).
- ⁶ C. A. Angell, *J. Res. Natl. Inst. Stand. Technol.* **102**, 171 (1997).
- ⁷ X. H. Lin, W. L. Johnson, and W. K. Rhim, *Mater. Trans. JIM*, **38**, 44 (1997).
- ⁸ S. C. Glade, R. Busch, D. S. Lee, W.L. Johnson, *J. Appl. Phys.*, **87**, 7242 (2000).
- ⁹ Y. J. Kim, R. Busch, W. L. Johnson, A. J. Rullison, and W. K. Rhim, *Appl. Phys. Lett.* **65**, 2136 (1994).
- ¹⁰ N. Nishiyama and A. Inoue, *Mater. Trans. JIM* **31**, 1531 (1996)
- ¹¹ I. R. Lu, G. Wilde, G. P. Görler, and R. J. Wittnecker, *J. Non-Cryst. Solids*, **577**, 250-252, (1999).
- ¹² Klement, W., Willens, R. H., and Duwez, P., *Nature*, **187**, 869-872 (1960).
- ¹³ T. Zhang, A. Inoue, and T. Masumoto, *J. Mater. Sci.*, **12**, 700-701, (1993).
- ¹⁴ D. Turnbull and M. H. Cohen, *Nature*, **189**, 131 (1961).
- ¹⁵ A. Inoue, *mater. Trans. JIM*, **36**, 866 (1995).
- ¹⁶ A. L. Greer, *Science*, **267**, 1947, (1995).
- ¹⁷ H. S. Chen and D. Turnbull, *J. Chem. Phys.*, **48**, 2560 (1968).
- ¹⁸ G. S. Grest and M. H. Cohen, *Adv. Chem. Phys.* **48**, 455, (1981).
- ¹⁹ J. Jäckle, *Rep. Prog. Phys.* **49**, 171, 1986.
- ²⁰ H. N. Ritland, *J. Amer. Ceram. Soc.*, **37**, 370 (1954).
- ²¹ H. Vogel, *phys. Z.*, **22**, 645 (1921)
- ²² G. S. Fulcher, *J. Am. Ceram. Soc.*, **6**, 339 (1925)
- ²³ G. Adams and J. H. Gibbs, *J. Chem. Phys.*, **43**, 139 (1965).
- ²⁴ M. D. Ediger, C. A. Angell, S. R. Nagel, *J. phys. Chem.*, **100**, 13200, (1996).
- ²⁵ J. Schroers, R. Busch, and W. L. Johnson, *Appl. Phys. Lett.*, **77**: 1158 (2000).
- ²⁶ R. Busch, E. Bakke, and W. L. Johnson, *Acta Metal.*, **46**, 4725 (1998).
- ²⁷ R. Böhmer, K. L. Ngai, C. A. Angell, and D. J. Plazek, *J. Chem. Phys.* **99**, 4201 (1993).
- ²⁸ B. Erwin, research proposal Materials Science and Engineering, Pennsylvania State University, (2002).
- ²⁹ J. A. Bucaro and H. D. Dardy, *J. Non-Cryst. Solids*, **24**, 121 (1977).
- ³⁰ K. L. Ngai, J. Colmenero, A. Alegria, and A. Arbe, *Macromolecules*, **25**, 4915 (1992).
- ³¹ R. Böhmer and C. A. Angell, *Phys. Rev. B* **45**, 10091 (1992).
- ³² R. Busch, W. Liu, and W.L. Johnson, *J. Appl. Phys.*, **83**, 4134 (1998).
- ³³ S. J. B. Reed, *Electron Microprobe Analysis and Scanning Electron Microscopy in Geology*, (Cambridge University Press, New York, 1996).

- ³⁴ C.C. Hays, J. Schroers, U. Geyer, S. Bossuyt, N. Stein and W. L. Johnson, *Mat. Sci. Forum*, **103**, **343-346**, (2000).
- ³⁵ T. B. Massalski, *Binary Alloy Phase Diagrams*, 2nd ed. (ASM International, Metals Park, OH, 1990).
- ³⁶ J. Saida and A. Inoue, *J. Phys.: Condens. Matter* **13**, L73-L75, (2001).
- ³⁷ F. Aubertin, S. Campbell, U. Gonser, *Hyperfine Interactions*, **28**, 997 (1986).
- ³⁸ PDF - 2 Database sets 1-49 and 70-86, PCPDFWIN Version 2.02, JCPDS-ICDD International Centre for Diffraction Data, (1999).
- ³⁹ A. Zhalko-Titarenko, *Phys. Status Solidi B*, **184**, 121 (1994).
- ⁴⁰ Wilson, *Acta Crystallogr.* **13**, 56 (1960).
- ⁴¹ T. Waniuk, J. Schroers, and W. L. Johnson, *Phys. Rev. B*. (publish pending).
- ⁴² A. Masuhr, T. A. Waniuk, R. Busch, and W.L. Johnson, *Phys. Rev. Lett.* **82**, 2290 (1999).
- ⁴³ A. Inoue, T. Zhang, and T. Masumoto, *Mater. Trans., JIM* **31**, 177 (1990).